RSC Advances

PAPER

View Article Online
View Journal | View Issue

Cite this: *RSC Adv.*, 2026, **16**, 19779

Eggshell-derived hydroxyapatite-alkali-activated waste glass composite for fluoride sequestration: characteristics and mechanistic insights and process optimization

Bennet Edem Akorley, *[ab] Ohene B. Apea[a] and Girum Ayalneh Tiruye *[b]

This study reports the development of a sustainable alkali-activated glass-hydroxyapatite composite (AAC-P@HAp) synthesized entirely from waste-derived precursors, including post-consumer glass bottles, eggshells, and plantain bunch stalk ash (as an alkali source), for fluoride removal from aqueous systems. The composite was produced through controlled alkali activation of micronized waste glass followed by hydrothermal-assisted integration of eggshell-derived hydroxyapatite within the aluminosilicate matrix. FTIR, XRF, SEM-EDX, and XRD confirmed successful composite formation of a hybrid silicate-phosphate material and revealed fluoride-induced changes in Ca–P domains after adsorption, indicating strong adsorbent–adsorbate interactions and chemical immobilization. Batch adsorption experiments demonstrated rapid fluoride uptake, with kinetic behavior adequately described by the pseudo-first-order model, while equilibrium data were better represented by the Freundlich isotherm, consistent with heterogeneous surface binding dominated by chemisorption. Thermodynamic analysis indicated that fluoride adsorption was spontaneous and endothermic. Within the Box–Behnken experimental domain, AAC-P@HAp achieved stable fluoride removal efficiencies in a narrow range (83–87%), with pH exerting the dominant influence on performance. Regeneration tests showed good initial reusability followed by a progressive decline attributed to irreversible chemisorption and depletion/phase transformation. In all, the results demonstrate the feasibility of converting multiple waste streams into a robust composite adsorbent and highlights AAC-P@HAp as a circular-economy-oriented material for secure fluoride immobilization rather than extensive multi-cycle reuse.

Received 18th January 2026
Accepted 21st March 2026

DOI: 10.1039/d6ra00457a

rsc.li/rsc-advances

1. Introduction

Fluoride contamination in water sources remains a persistent global concern due to its adverse impacts on human health and ecosystems.[1–3] While fluoride is beneficial at trace concentrations, excessive intake through drinking water poses serious health risks and environmental challenges. Consequently, controlling fluoride concentrations in water supplies is a critical issue, particularly in regions that rely heavily on groundwater resources.

Fluoride occurs naturally in minerals such as fluorite, fluorapatite, topaz, and cryolite, and geological processes including mineral weathering and dissolution can release fluoride into groundwater, especially in fluoride-rich lithological settings.[1,4–7] In addition to geogenic sources, anthropogenic activities such as aluminum smelting, phosphate fertilizer production, coal combustion, and industrial effluent discharge are sources that contribute substantially to environmental fluoride loading.[1,8]

Chronic consumption of fluoride-contaminated water is strongly associated with dental and skeletal fluorosis, characterized by enamel damage, joint pain, bone stiffness, and skeletal deformities.[9] Emerging evidence further indicates potential neurodevelopmental effects. A recent meta-analysis published in JAMA Pediatrics reported a statistically significant association between fluoride exposure and reduced cognitive performance in children, with a decrease of 1.63 IQ points per 1 mg L^{-1} increase in urinary fluoride.[10] Elevated fluoride levels also disrupt metabolic processes in aquatic organisms and impair plant growth, posing risks to both aquatic and terrestrial ecosystems.

Globally, fluoride contamination is particularly prevalent in groundwater dependent regions across Africa, Asia, and the Americas, where concentrations frequently exceed the World Health Organization guideline value of 1.5 mg L^{-1}.[1] Addressing this challenge is therefore essential for achieving UN Sustainable Development Goal (SDG) 6 (Clean Water and Sanitation) and SDG 3 (Good Health and Well-Being).

[a]*Department of Applied Chemistry, C. K. Tedam University of Technology and Applied Sciences, Ghana. E-mail: bennetakorley@gmail.com*

[b]*Center for Materials Science and Engineering, College of Natural and Computational Sciences, Addis Ababa University, P.O.Box 1176, Addis Ababa, Ethiopia. E-mail: girum.ayalneh@aau.edu.et*

Among available treatment technologies, adsorption is widely regarded as one of the most practical approaches for fluoride removal due to its operational simplicity, adaptability, and effectiveness over a broad range of water chemistries. However, many conventional fluoride adsorbents suffer from sustainability limitations, which includes high production costs, dependence on virgin raw materials, and environmental burdens associated with synthesis and disposal. These limitations conflict with SDG 12 (responsible consumption and production).

In response, growing attention has been directed toward the development of adsorbents derived from waste materials within a circular economy framework. Industrial by-products and agricultural residues such as slag, petroleum coke, and biomass-derived biochar, which of recent reports have demonstrated promising adsorption performance while simultaneously reducing waste disposal pressures and environmental footprints.[11–14]

Within this sustainability driven context, alkali-activated materials (AAMs) have emerged as attractive candidates for environmental remediation. Waste glass is particularly appealing due to its high silica content, global abundance and underutilization. Despite the generation of millions of tons of post-consumer glass annually, a substantial fraction is landfilled, representing a lost opportunity for value-added reuse.[15,16] When alkali-activated, waste glass forms a geopolymer-like aluminosilicate matrix with favourable mechanical stability, chemical durability, and surface functionality suitable for adsorption-based water treatment.[16–19]

However, pristine alkali-activated glass systems are known to exhibit limited affinity towards anionic contaminants, including fluoride, due to their predominantly negatively charged aluminosilicate frameworks and lack of specific binding sites.[20] Consequently, waste glass-based AAMs and their modified forms have been more successfully applied for the removal of cationic species, such as heavy metals and dyes, as consistently reported in literature.[21–26] This intrinsic limitation restricts their direct application for anionic pollutant removal and underscores the need for strategic functional modification.

The environmental footprint of alkali activation is also strongly influenced by the choice of activator. Conventional alkalis such as sodium or potassium hydroxide are effective but energy-intensive. To enhance sustainability, alternative alkali sources derived from agricultural residues have gained increasing attention. In this study, alkali extracted from plantain bunch stalk ash is employed as a greener activating agent, simultaneously valorizing agricultural waste while reducing reliance on synthetic chemicals.

To overcome the limited anion adsorption capacity of pristine alkali-activated glass while preserving its sustainability advantages, the present work adopts a hybrid material design strategy. Hydroxyapatite (HAp) is well known for its strong affinity toward fluoride ions due to its calcium- and phosphate-rich structure, which enables ion exchange, surface complexation and lattice substitution mechanisms.[27–29] Nevertheless, most reported HAp-based adsorbents rely on energy-intensive synthesis routes, nano-scale powders, or standalone HAp phases that may suffer limited mechanical stability, aggregation and scalability.

Waste eggshells, composed predominantly of calcium carbonate, offer an abundant and biogenic calcium source for sustainable hydroxyapatite production. Rather than employing HAp as a standalone sorbent, this study integrates a small quantity of eggshell-derived hydroxyapatite into an alkali-activated waste glass matrix, thereby extending the functional scope of the base material from predominantly cationic pollutant removal towards anionic fluoride adsorption.

It is important to clarify the design philosophy of the present AAC-P@HAp system in relation to calcium-rich alkali-activated composites previously reported by our group.[16] The previously reported AAC-P@Ca system was deliberately engineered as a capacity-maximized adsorbent, where fluoride removal is dominated by rapid Ca^{2+} dissolution followed by precipitation/complexation reactions. While CaO-rich AAC-P materials have demonstrated very high fluoride uptake capacities (>40 mg g^{-1}) due to their high alkalinity and highly reactive calcium sites, such systems are primarily optimized for capacity maximization and precipitation-dominated removal. In contrast, the present work does not seek to outperform this material in terms of gravimetric fluoride capacity. Instead, the conversion of reactive CaO into hydroxyapatite represents a deliberate strategy to chemically stabilize calcium within a calcium-phosphate lattice, enabling controlled fluoride immobilization through surface complexation and lattice substitution mechanisms.

Compared with CaO-based systems, hydroxyapatite exhibits significantly greater chemical stability in aqueous environments because calcium ions are incorporated within a stable calcium-phosphate lattice rather than existing as highly soluble CaO phases.[30–32] CaO readily hydrates and dissolves to release Ca^{2+} and OH^{-}, which can lead to uncontrolled precipitation reactions and elevated alkalinity in treated water.[33] In contrast, hydroxyapatite demonstrates lower dissolution rates and enables fluoride immobilization primarily through hydroxyl-fluoride exchange and fluorapatite formation within the apatite lattice.[34] Previous studies have further shown that hydroxyapatite maintains structural integrity and limits calcium release during aqueous reactions compared with CaO-based sorbents, thereby improving chemical stability and environmental compatibility.[35]

Although AAC-P@Ca provides higher fluoride uptake, its removal mechanism relies on highly alkaline conditions and significant Ca^{2+} mobility, which may result in elevated alkalinity, greater dissolution and leaching, and precipitation-dominated removal with limited long-term stability or regeneration potential. To address these limitations, CaO was converted into hydroxyapatite (HAp), a thermodynamically stable calcium-phosphate phase that immobilizes calcium within a crystalline lattice, reduces uncontrolled Ca^{2+} release, promotes fluoride incorporation *via* hydroxyl-fluoride exchange and fluorapatite formation, and improves structural integrity and environmental compatibility. Thus, the present system prioritizes stability, controlled reactivity, and secure fluoride fixation rather than maximum adsorption capacity.

Against this backdrop, the present study introduces a fully waste-derived hybrid alkali-activated glass-hydroxyapatite composite (AAC-P@HAp) synthesized entirely from waste-derived precursors, including post-consumer glass bottles, plantain bunch stalk ash as a bio-alkali activator, and eggshell-derived calcium. In this composite, calcium-phosphate domains are embedded within a chemically robust aluminosilicate matrix, forming a hybrid silicate-phosphate interface that combines surface accessibility, structural integrity, and chemical reactivity. This design could enable synergistic fluoride removal through combined electrostatic attraction, hydroxyl-fluoride ion exchange, and inner-sphere complexation at Ca-rich sites, while maintaining low material cost and reduced environmental footprint. In this study, the structural integration characteristics, adsorption performance, process optimization using Box–Behnken design, regeneration behavior, and fluoride adsorption mechanisms of AAC-P@HAp are systematically investigated using FTIR, XRD, SEM-EDX, and surface charge analyses. By integrating multiple waste streams into a single functional adsorbent, and addressing the inherent limitations of waste glass-based adsorbents for anionic pollutants, this work advances sustainable defluoridation strategies aligned with circular economy principles and the United Nations Sustainable Development Goals.

2. Materials and methods

2.1. Materials and chemicals

Post-consumer waste glass bottles, poultry eggshells, and plantain bunch stalks were used as precursor materials for composite synthesis. All chemicals used in this study include sodium fluoride (NaF, ≥99%), trisodium citrate (≥99%), sodium chloride (NaCl, ≥99.5%), ethylenediaminetetraacetic acid (EDTA, ≥99%), acetic acid (CH_3COOH, ≥99.7%), sodium hydroxide (NaOH, ≥98%), hydrochloric acid (HCl, 37%), silver nitrate ($AgNO_3$, ≥99.9%), phosphoric acid (H_3PO_4, 85%), and potassium hydrogen phosphate (KH_2PO_4, ≥98%). All reagents were of analytical grade and used without further purification.

2.2. Preparation of alkaline solution from plantain bunch stalks

The alkaline activating solution was prepared from plantain bunch stalks following our previously reported methodology as part of ongoing work on waste-derived alkali systems.[16] The physicochemical properties of the resulting alkaline extract, including alkalinity, electrical conductivity, effective alkali purity and ionic composition determined by ICP-OES, are summarized in Table 1 and 2. Fresh plantain bunch stalks (5130.19 g) were thoroughly cleaned and air-dried to constant mass, yielding 199.28 g of dry biomass (Table 1). This corresponds to a moisture content of 97.68% and a dry mass content of 2.32% on a fresh-weight basis.

The dried biomass was subjected to controlled combustion, producing 59.796 g of charcoal and 30.668 g of ash, corresponding to an ash content of 25.71% on a dry basis. For the alkaline extraction, 200 g of ash was mixed with 800 mL of deionized water.[16,36,37] The resulting suspension was decanted, filtered and the clear supernatant collected as the bio-derived alkaline solution used for alkali activation of powdered waste glass.

Table 1 Physicochemical properties of plantain bunch stalk ash derived alkaline extract

Parameter	Value
Moisture content (%)	97.68
Dry matter content (%)	2.32
Ash content (dry basis, %)	25.71
Alkali extraction yield (%)	86.67
Alkali concentration (mol dm^{-3})	1.285 ± 0.023
Estimated KOH equivalent (g)	23.31 ± 0.022
Estimated NaOH equivalent (g)	0.132 ± 0.002
pH	11.403 ± 0.032
Electrical conductivity (μS cm^{-1})	195.9 ± 0.042
Effective alkali purity (%)	61.76

2.3. Preparation of alkali-activated glass ceramic adsorbent (AAC-P)

The synthesis of alkali-activated waste glass (AAC-P) was carried out following a previously reported procedure with minor modifications (Akorley *et al.*, Chemical Engineering Journal Advances, 2026).[16] Briefly, post-consumer waste glass bottles were thoroughly washed, dried, and milled using a planetary ball mill to obtain particles with sizes below 75 μm as in Fig. 1a.

The bulk chemical composition of the waste glass precursor, determined by XRF analysis, is summarized in Table 3. The glass is predominantly composed of SiO_2 (86.24 wt%) and CaO (10.43 wt%), with minor contributions from Al_2O_3, MgO and Fe_2O_3, making it suitable for alkali activation and geopolymer-like network formation.

Alkali activation was achieved using an alkali extract derived from plantain bunch stalk ash as in Fig. 1b, prepared according to the method described in our earlier work.[16] For activation, 60 g of glass powder was mixed with 40 mL of the bio-derived alkali solution, corresponding to a liquid-to-solid ratio of 0.67 mL g^{-1}. This ratio was selected based on preliminary trails to ensure sufficient alkalinity for glass dissolution while maintaining workable slurry consistency.

The mixture was homogenized to dorm a uniform slurry and cured under ambient conditions. After curing, the solid product

Table 2 Dissolved ionic composition of plantain bunch stalk ash-derived alkaline solution (ICP-OES analysis)

Element	Concentration (ppm)	Ionic fraction (%)
K	22 808.31	61.35
Fe	8972.00	24.13
Zn	2695.00	7.25
Ag	2127.00	5.72
Cu	264.00	0.71
Na	150.06	0.40
Pb	133.00	0.36
Ca	23.83	0.06
Mg	1.71	0.005
Total	37 174.91	100.00

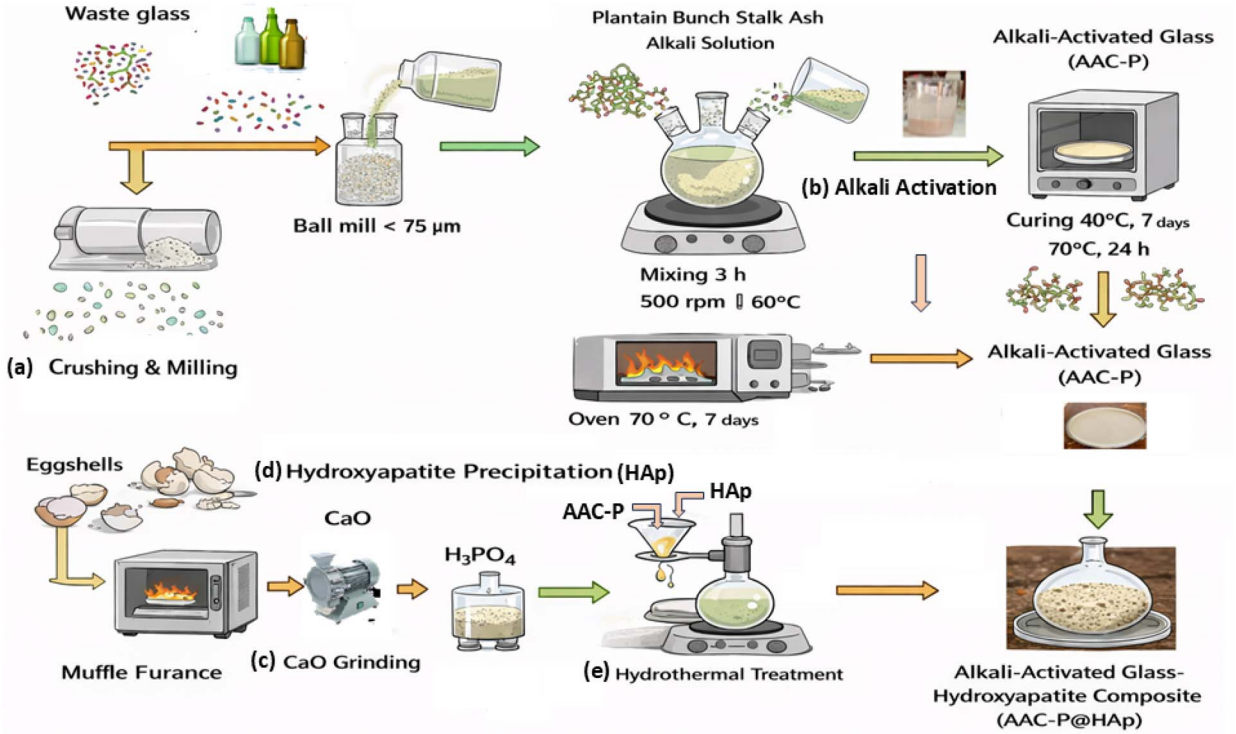

Fig. 1 Schematic representation of waste glass alkali-activation leading to reactive glass-ceramic precursors. (a) Crushing and milling of waste glass, (b) alkali activation process, (c) CaO preparation, and (d and e) hydroxyapatite synthesis.

Table 3 Bulk oxide composition of recycled waste glass precursor (XRF analysis)[a]

Oxide	Content (wt%)
SiO_2	86.24
CaO	10.43
Al_2O_3	1.79
MgO	1.18
Fe_2O_3	0.64
ZnO	0.012
PbO	0.051
Loss on ignition (LOI)	8.35

[a] NB: LOD is limit of detection.

was repeatedly washed with deionized water to remove excess alkali, followed by drying to obtain the alkali-activated glass ceramic adsorbent (AAC-P).

The use of wase-derived alkali and explicitly defined mass-to-volume ratios ensures reproducibility of the synthesis process and supports the sustainable valorization of agricultural and post-consumer waste streams.

2.4. Synthesis of eggshell-derived hydroxyapatite (HAp)

Calcium phosphate (hydroxyapatite was synthesized at room temperature by precipitation method.[38] Poultry eggshells collected from restaurants around the Arat Kilo area, Addis Ababa, Ethiopia were pretreated by washing with boiled deionized water for few minutes to remove the surface contaminants. To eliminate organic materials and convert $CaCO_3$ to CaO, the eggshells were heated in a maffle furnace at 1000 °C for 4 hours (Fig. 1c).

The CaO was milled with micro-planetary grinding machine (FZ102, China). The calcium phosphate was prepared with 31 g of CaO dissolved in 500 mL deionized water at 60 °C for 30 minutes while stirring with magnetic stirrer. The H_3PO_4 (0.6 M) was added to the hydrolyzed CaO in a rate of 3.33 mL min^{-1} till precipitate is formed. The mixture was stirred at 80 °C and the pH was adjusted with HCl acid to 9.5. The precipitate was washed with deionized waster, filtered and dried at 200 °C for 4 hours to give hydroxyapatite (HAp) as shown in Fig. 1d.

2.5. Preparation of alkali-activated glass-hydroxyapatite composite (AAC-P@HAp)

The AAC-P@HAp composite was prepared *via* a hydrothermal-assisted integration process. AAC-P was dispersed in deionized water and thermally activated at 60 °C for 120 minutes, after which eggshell-derived hydroxyapatite was introduced at a fixed mass ratio (AAC-P:HAp, 3 : 1 *i.e.*, 30 g : 10 g). The mixture was maintained under controlled temperature and stirring conditions to promote interfacial interaction between AAC-P and HAp for additional 180 minutes. The composite formed was then filtered, washed, and dried to obtain the final adsorbent (AAC-P@HAp) as in Fig. 1e.

2.6. Preparation of adsorbate

All reagents used for adsorbate preparation were of analytical grade. A 1000 mg L^{-1} NaF stock solution was prepared in

deionized water and diluted as needed. Total Ionic Strength Adjustment Buffer (TISAB III) was used in all fluoride measurements to maintain consistent ionic strength and pH.

2.7. Physicochemical characterization of materials

The acid-base potentiometric titration method used as described by[39] with slight modifications as follows. The adsorbent materials of 1 g of weight were kept in a 20 ml of 0.002 M potassium chloride (KCl) electrolyte and equilibrated for approximately 18 hours through horizontal shaking with Faithful multifunctional water bath shaker FWS-30, China at 200 rpm and 25 °C. The initial pHs of suspension were varied using 0.1 M of hydrochloric acid (HCl) and sodium hydroxide (NaOH) while the blank suspensions contained no acid or base. The pH of suspensions was measured after each subsequent addition and equilibration with 0.1 (1 mL) KCl and 2 M (0.5 mL) KCl. The amount of potential determining ions (H^+/OH^-) adsorbed was estimated as the pH difference between the blank and acid/base titrated suspensions at each different KCl concentration using Hanna H15522 pH mV/ISE/EC/TDS/Salinity/Resistivity meter, Thailand.

Bulk density was calculated from the mass-to-volume ratio of packed samples.[39] The pH and electrical conductivity (EC) of the absorbent suspensions (1 g in 20 mL deionized water) were measured after 48 hours equilibrium using Hanna H15522 pH mV/ISE.EC/TDS/Salinity/Resistivity meter, Thailand.

The materials were comprehensively characterized to evaluate their surface chemistry, morphology, elemental composition, textural properties, and crystalline phases. Surface functional groups and chemical bonding environments were identified by Fourier-transform infrared (FTIR) spectroscopy using a PerkinElmer Spectrum 65 spectrometer (PerkinElmer Inc., USA). FTIR spectra were recorded in the wavenumber range of 400–4000 cm^{-1}. Phase composition and crystallographic structure were analyzed by X-ray powder diffraction (XRD) employing a Rigaku Miniflex 600 diffractometer (Rigaku Corporation, Japan). Diffractograms were collected over a 2θ range of 10–80° using CuKα radiation to assess phase purity and crystallinity.

Surface morphology and elemental distribution of the materials before and after fluoride sequestration were examined using scanning electron microscopy (SEM) coupled with energy-dispersive X-ray spectroscopy (EDS). SEM observations were performed with a Coxem CX-200tA microscope (Coxem Co., South Korea), while EDS analysis provided qualitative and semi-quantitative elemental composition. The specific surface area of the samples was determined by nitrogen adsorption measurements using the Brunauer–Emmett–Teller (BET) method with an SA-9600 series surface area analyzer (HORIBA Instruments Inc., Japan). Prior to analysis, samples were degassed under appropriate conditions to remove physically adsorbed species. The bulk elemental composition and oxide distribution of the AAC-P@HAp material were determined by X-ray fluorescence (XRF) spectroscopy using a Niton XL2 analyzer (Thermo Fisher Scientific, USA).

2.8. Batch adsorption experiments

Batch adsorption experiments were conducted to evaluate the fluoride removal performance of the AAC-P@HAp composite under controlled conditions. All adsorption tests were performed in 100 mL conical flasks containing 50 mL of fluoride solution and agitated in a thermostatic water bath shaker at 150 rpm. After the adsorption process, the solid and liquid phases were separated by filtration, and the residual fluoride concentration in the supernatant was determined using a fluoride ion-selective electrode (CRISON GLP 22, Spain) (Fig. 2a). All experiments were carried out in triplicate, and average values were reported.

The influence of significant operational parameters on fluoride sequestration was systematically investigated by varying one parameter at a time while keeping the others constant. Adsorbent dosage was varied between 0.5 and 5.0 g L^{-1} using an initial fluoride concentration of 25 mg L^{-1} to determine the optimal dosage (Fig. 2b). Adsorption kinetics were evaluated by varying the contact time from 2 to 150 min at a fixed adsorbent dose (1.0 g L^{-1}) and fluoride concentration (100 mg L^{-1}) at 30 °C. The effect of solution pH was examined over the pH range of 2.5–10.5 using buffered fluoride solutions (50 mg L^{-1}), while maintaining constant adsorbent dose and contact time. The influence of temperature was studied in the range of 30–80 °C at pH 3.5, and the effect of initial fluoride concentration was assessed by varying fluoride concentrations from 10 to 100 mg L^{-1} under optimized experimental conditions.

To evaluate the effect of competing ions, adsorption experiments were conducted in the presence of common co-existing ions (NaCN and K_2SO_4) at concentrations ranging from 10 to 60 mg L^{-1} using both binary and ternary ion systems. These experiments were designed to simulate competitive adsorption conditions commonly encountered in natural water systems.

The adsorption capacity (q_e, mg g^{-1}) and fluoride removal efficiency (%) were calculated using the following equations:

$$q_e = \frac{(C_0 - C_e)V}{m} \quad (1)$$

$$\text{Removal } (\%) = \frac{(C_0 - C_e)}{C_0} \times 100 \quad (2)$$

where $C_0$and $C_e$are the initial and equilibrium fluoride concentrations (mg L^{-1}), $V$is the volume of the solution (L), and the mass of the adsorbent (g).

The reusability of AAC-P@HAp was evaluated through successive adsorption–desorption cycles to assess its operational stability and practicability (Fig. 2c). Following fluoride sequestration, the spent adsorbent was separated by filtration. Regeneration was carried out by dispersing the recovered adsorbent (2 g) in 50 mL of 0.1 M NaOH solution and agitating the suspension on a magnetic hotplate stirrer at 150 rpm and 30 °C for 3 h to promote fluoride desorption. After regeneration, the adsorbent was washed three consecutive times with deionized water to remove excess alkali, dried at 70 °C for 12 h, and subsequently reused under identical adsorption conditions (initial fluoride concentration of 25 mg L^{-1}, contact time of 60 min). This procedure was repeated for six consecutive cycles to evaluate regeneration efficiency and performance stability.

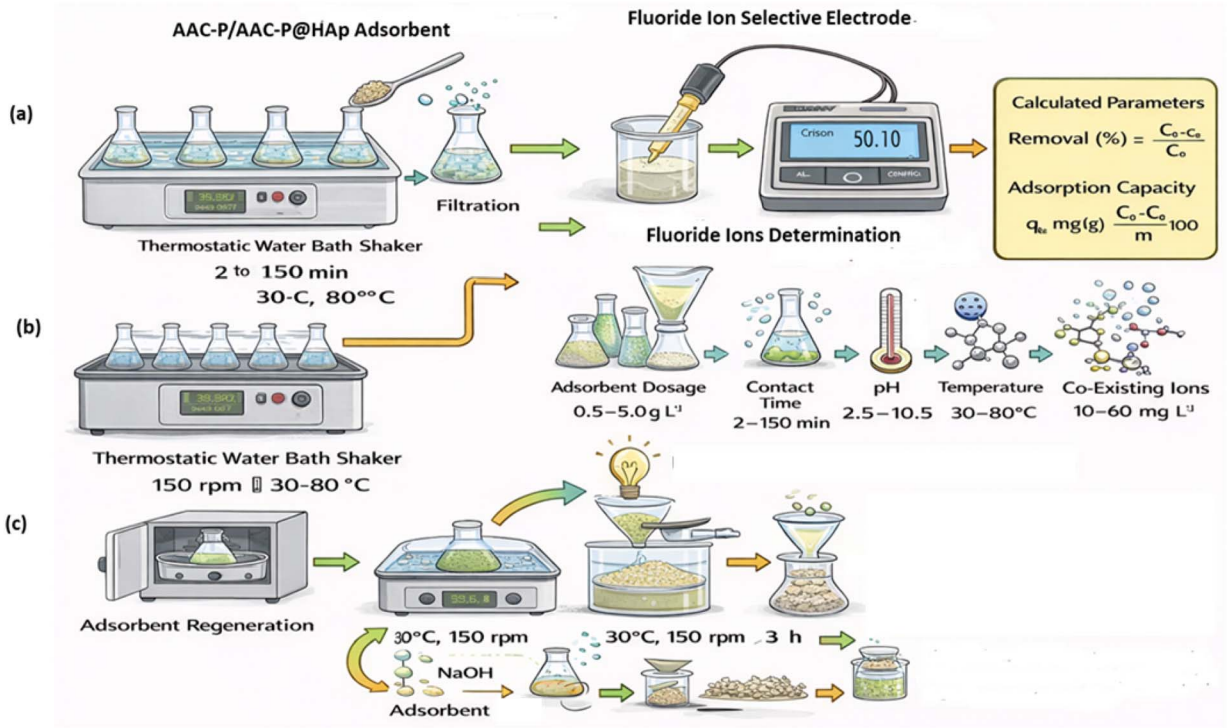

Fig. 2 Schematic illustration of the adsorption process: (a) experimental setup, (b) effects of operational parameters, and (c) regeneration studies.

2.9. Adsorption kinetics and thermodynamic analysis

The adsorption kinetics of fluoride onto the AAC-P@HAp composite were evaluated using the pseudo-first-order (PFO) and pseudo-second-order (PSO) kinetic models to describe the rate and mechanism of the adsorption process.[40,41] The experimental kinetic data obtained from batch adsorption experiments were fitted to the following equations:

$$\ln (q_e - q_t) = \ln q_e - k_1 t \quad (3)$$

$$\frac{t}{q_t} = \frac{1}{k_2 q_e^2} + \frac{t}{q_e} \quad (4)$$

where q_t(mg g^{-1}) is the amount of fluoride adsorbed at time t(min), q_e(mg g^{-1}) is the adsorption capacity at equilibrium, k_1(min^{-1}) is the pseudo-first-order rate constant, and k_2(g mg^{-1} min^{-1}) is the pseudo-second-order rate constant.

The thermodynamic feasibility and nature of the fluoride adsorption process were assessed by evaluating the changes in Gibbs free energy (ΔG°), enthalpy (ΔH°), and entropy (ΔS°) based on temperature-dependent adsorption data.[42] The thermodynamic parameters were calculated using the following relationships:

$$\Delta G^\circ = -RT \ln K_d \quad (5)$$

$$\ln K_d = \frac{\Delta S^\circ}{R} - \frac{\Delta H^\circ}{RT} \quad (6)$$

where $R$is the universal gas constant (8.314 J mol^{-1} K^{-1}), $T$is the absolute temperature (K), and $K_d$is the distribution coefficient defined as $K_d = q_e/C_e$, with C_e(mg L^{-1}) representing the equilibrium fluoride concentration.

2.10. Optimization approach (Box–Behnken method)

The optimization of fluoride adsorption parameters requires a well-planned experimental methodology to assures robust and objective conclusion bearing in mind the cost. Box and Behnken (1960) proposed a different experimental design for second-order models, permitting the estimation of certain interactions.[43] The main worth of experimental designs is that they reduce the number of experiments needed during the testing phase of determining possible factors or combinations of factors which could impact the response of the system under study.[44] In the current studies, the effect of three factors on the adsorption efficiency which is important for enhancing the effectiveness of the adsorption process, namely adsorbent dose (X_1), temperature (X_2) and pH X_3). The ranges and levels of these variables were determined based on the preliminary study as indicated in Table 4 as coded and actual values. Each variable was assessed in three different levels: −1, 0, and 1.[45]

The mathematical model (eqn (7)) adopted is a second-degree polynomial, which establishes correlation between dependent and independent variables.

$$Y = \beta_0 + \sum_{i=1}^{n} (\beta_i x_i) + \sum_{i=1}^{n} (\beta_{ii} x_i^2) \sum_{i=1}^{n} (\beta_{ii} x_i^2) + \sum_{i=1}^{i=1} \sum_{j=1}^{i=1} (\beta_{ij} x_i x_j) \quad (7)$$

Table 4 Experimental variables, coded levels, and design matrix of the Box–Behnken methodology

Variables	Levels		
Coded levels	−1	0	+1
X_1: Adsorbent dose (g L^{-1})	303	313	323
X_2: Temperature (K)	0.5	2	3.5
X_3: pH	3.5	6	10.5

where, Y is the response function, β_0 is the polynomial constant expressing the general mean effect, β_i, β_{ii}, and β_{ij} are the coefficient of the linear, quadratic and interaction effects, respectively, x_i and x_j represent the independent coded variables.

Following the Box–Behnken design, the 15 experiments between AAC-P@HAp adsorbent and fluoride adsorbate were carried out by varying the three variables (X_1), (X_2) and (X_3) to determine the optimum response surface. The response parameters were considered as the percentage of removal efficiency (Y). Analysis of variance (ANOVA) was used to establish the coefficients essential for the interpreting and validating the results.

3. Results and discussion

3.1. Physicochemical characterizations of as-synthesized composite materials

The physicochemical properties of the synthesized materials, including surface pH, point of zero charge (pH_{PZC}), electrical conductivity, and bulk density, were determined to elucidate their surface charge behavior, ionic mobility, and structural compactness, which are critical parameters governing adsorption performance. The measured properties of AAC-P, AAC-P@HAp, and the spent AAC-P@HAp after fluoride sequestration are summarized in Table 5.

Table 5 Key physicochemical parameters of the prepared adsorbents (pH, point of zero charge, bulk density, and electrical conductivity)

Parameter	AAC-P	AAC-P@HAp	Spent AAC-P@HAp
pH_{PZC}	10.35 ± 0.014	10.56 ± 0.032	7.00 ± 0.011
pH	10.417 ± 0.012	10.717 ± 0.006	—
E.C	1054.5 ± 1.5	1098.5 ± 0.5	
Bulk density	1.2 ± 0.0333	1.143 ± 0.0289	

The AAC-P@HAp exhibits a highly alkaline surface with a pH_{pzc} of 10.56, indicating that the surface remains positively charged over a wide pH range. Such alkaline character is particularly favorable for the adsorption of anionic species such as fluoride due to enhanced electrostatic attraction between negatively charged fluoride ions and positively charged surface sites.[46] The elevated pH_{pzc} is attributed to the combined presence of calcium-rich hydroxyapatite and alkali-activated silicate phases, which introduce abundant hydroxyl and phosphate functional groups (Table 6).

The equilibrium suspension pH (10.717) further confirms the dominance of basic surface functionalities. Hydroxyapatite contributes Ca–OH and PO_4^{3-} surface groups that could promote ion exchange and surface complexation mechanisms, particularly hydroxyl-fluoride exchange and calcium–fluoride interactions during adsorption. These processes are widely reported to enhance fluoride uptake in alkaline environments.[29,47–50]

The electrical conductivity of AAC-P@HAp (1098.5 μS cm^{-1}) reflects the presence of mobile ionic species within the composite matrix, which could originate from alkali-activated glass phases and partially soluble calcium–phosphate species. This enhanced ionic mobility could facilitate surface reactions and mass transfer during adsorption. The relatively low bulk density (1.143 g cm^{-1}) indicates a loosely packed structure with increased void space, which could be attributed to hydroxyapatite incorporation disrupting dense packing within the alkali-activated matrix.[51]

3.2. Structure and chemical characteristics

The elemental oxide composition determined by X-ray fluorescence (XRF), together with the crystallographic features obtained from X-ray diffraction (XRD), provides complementary insight into the structural evolution of AAC-P upon hydroxyapatite (HAp) incorporation (Table 6 and Fig. 3a). As-synthesized AAC-P is dominated by SiO_2 (76.07 wt%) and exhibits a high Si/Al ratio of 40.06, an indication of a silica-rich alkali-activated glass network. Consistent with this composition, the XRD pattern of AAC-P (red peak) is characterized by a broad diffuse hump centered around $2\theta \approx 25$–$35°$, with no distinct sharp reflections.[52] This feature is typical of predominantly amorphous aluminosilicate gels formed during alkali activation of glassy precursors and confirms the absence of long-range crystalline order.

Table 6 XRF-derived oxide composition, Si/Al ratio, characteristic XRD reflections, and crystallinity of alkali-activated glass (AAC-P), hydroxyapatite-modified AAC-P (AAC-P@HAp), and pristine hydroxyapatite (HAp), illustrating phase evolution upon HAp incorporation[a]

Sample	SiO_2 (wt%)	Al_2O_3 (wt%)	P_2O_5 (wt%)	MgO (wt%)	Ag_2O (wt%)	Si/Al (XRF)	XRD characteristic reflection (2θ)	Crystallinity
AAC-P	76.07	1.90	<LOD	1.14	<LOD	40.06	Halo centred at ~30° (2θ)	Amorphous
AAC-P@HAp	46.12	1.79	47.26	1.14	0.204	25.76	~25.9° (002), 31.8° (211), 32.9° (300), 34.1° (112)	Semi-crystalline (~58.6%)
HAp	3.28	1.88	94.10	0.002	0.273	—	25.9° (002), 31.8° (211), 32.9° (300), 34.1° (112)	Highly crystalline (~98.34%)

[a] NB; LOD – Limit of Detection.

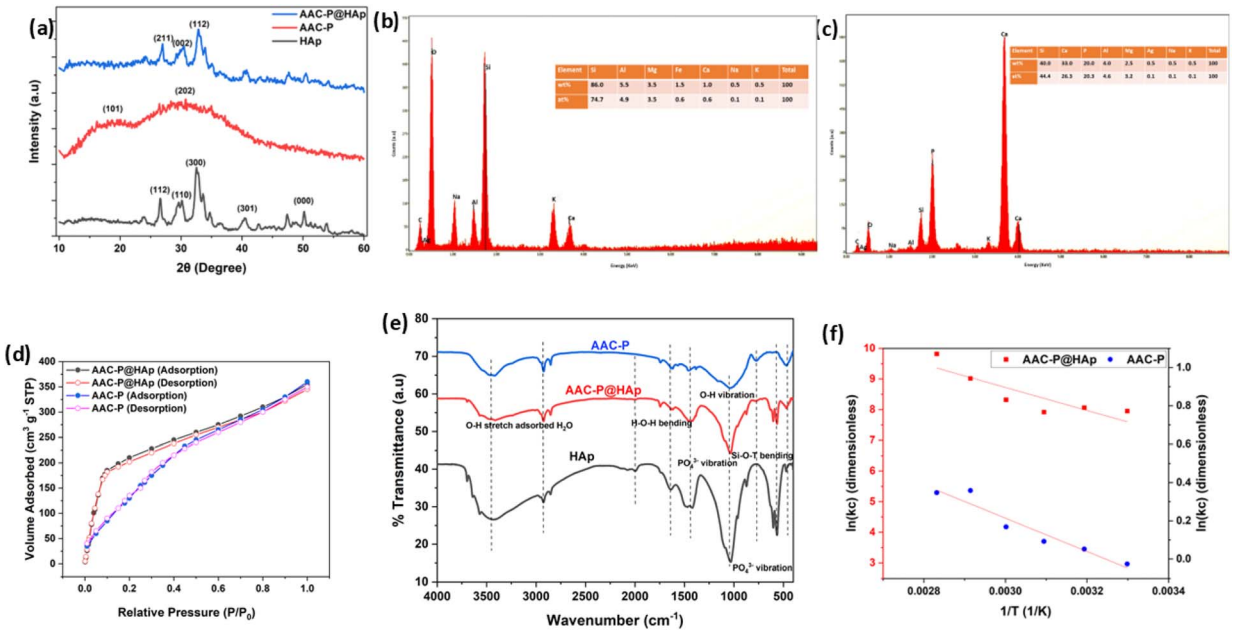

Fig. 3 (a) XRD diffraction pattern of synthesized adsorbent materials, (b) EDX peaks of the synthesized AAC-P adsorbent material, (c) EDX peaks of the synthesized AAC-P@HAp composite material, (d) N_2 adsorption–desorption isotherms of AAC-P and AAC-P@HAp adsorbent materials, (e) FTIR spectrum of synthesized AAC-P and AAC-P@HAp, (f) Van't Hoff plot of the sorption between fluoride ions and adsorbent materials.

In contrast, the XRD pattern (blue peak) of the AAC-P@HAp composite shows the emergence of distinct diffraction peaks superimposed on the amorphous background. The reflections observed at approximately $2\theta \approx 25.9°$, 31.8°, 32.9°, and 34.1° correspond well to the (002), (211), (300), and (112) crystallographic planes of hydroxyapatite, respectively (JCPDS No. 09-0432).[53] These peaks closely match those of the reference HAp pattern (black peak), confirming the successful formation and structural retention of hydroxyapatite within the alkali-activated glass matrix. The persistence of the broad amorphous halo alongside these reflections indicates that the alkali-activated aluminosilicate framework remains largely intact after HAp incorporation.

The compositional changes observed by XRF (Table 6) further support the XRD findings. Upon HAp addition, the SiO_2 content decreases to 46.12 wt%, while P_2O_5 increases sharply to 47.26 wt%, accompanied by an increase in CaO content (Fig. 3b and c). The reduction in the Si/Al ratio to 25.76 reflects the partial dilution of the silicate network by calcium-phosphate phases rather than structural degradation of the alkali-activated matrix. The coexistence of amorphous and crystalline phases results in a semi-crystalline composite with an estimated crystallinity of approximately 58.6%, arising primarily from the hydroxyapatite contribution.

Importantly, no diffraction peaks associated with secondary calcium-containing phases such as free CaO, tricalcium phosphate, or other calcium phosphates were detected. This suggests that calcium derived from eggshell waste was effectively incorporated into the hydroxyapatite structure rather than forming undesirable by-products. The XRD patterns confirm the formation and structural retention of crystalline hydroxyapatite within the composite. While diffraction data verify phase presence and crystallographic identity, they do not independently resolve the spatial distribution on HAp domains. Evidence for structural integration is supported by SEM morphology (Fig. 4d–f), which shows morphological modification of the alkali-activated matrix after HAp incorporation, and by EDX spectra (Fig. 3c), confirming the presence of Ca and P within the composite. The persistence of the amorphous aluminosilicate halo alongside distinct HAp reflections further suggests coexistence of amorphous and crystalline phases rather than complete phase segregation. However, definitive confirmation of nanoscale dispersion would require high-resolution techniques such as TEM.

3.3. Surface morphology and microstructure of the synthesized materials

The morphological and compositional evolution of AAC-P following hydroxyapatite (HAp) incorporation was investigated using scanning electron microscopy (SEM) coupled with energy-dispersive X-ray spectroscopy (EDX) (Fig. 3 and 4). The combined analyses provide insight into the structural reorganization and surface chemistry modifications relevant to fluoride sequestration.

SEM micrographs of synthesized AAC-P reveal a heterogeneous and porous morphology composed of irregularly shaped (Fig. 4a–c), loosely packed aggregates with rough surfaces and open inter-particle voids *i.e.* 1000× magnification (Fig. 4c). This texture, characteristic of alkali-activated glass-derived aluminosilicate materials, reflects a broad particle size distribution and the presence of accessible surface features. The average particle size of AAC-P was estimated to be approximately 31.85

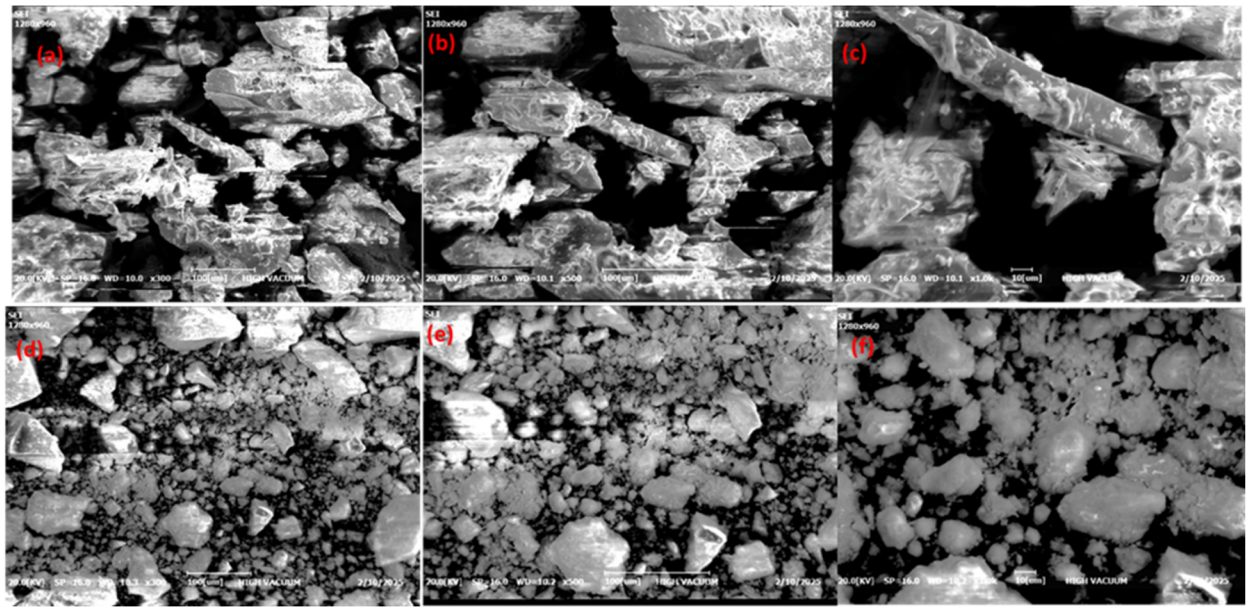

Fig. 4 SEM micrographs of the synthesized AAC-P adsorbent at (a) 300×, (b) 500×, and (c) 1000× magnifications, and the AAC-P@HAp composite at (d) 300×, (e) 500×, and (f) 1000× magnifications.

μm, consistent with the formation of agglomerates during alkali activation process.[54]

Following HAp incorporation, the AAC-P@HAp composite exhibits noticeable but moderate morphological changes (Fig. 4d–f). The surface becomes comparatively smoother and more compact *i.e.* 1000× magnification (Fig. 4f), with partial filling of surface voids and inter-aggregate spaces (Fig. 4d), suggesting deposition or *in situ* formation of HAp within the AAC-P matrix. This structural rearrangement is accompanied by a slight decrease in the average particle size to approximately 30.61 μm, likely resulting from enhanced packing density and improved inter-particle cohesion. The incorporation of hydroxyapatite leads to partial pore filling and surface smoothing, which is reflected in the observed reduction in BET surface area. Although this densification reduces accessible surface area and pore volume to some extent, it promotes greater surface uniformity and structural integrity of the composite.

The EDX analysis provides complementary compositional information for the pristine AAC-P and the AAC-P@HAp composite (Fig. 3b and c). The ACC-P spectrum is dominated by Na, Al, Si, O and C, which is consistent with the formation of an alkali-activated aluminosilicate matrix. The presence of these elements confirms the successful activation of the precursor and agrees well with the bulk compositional trends obtained from XRF analysis. Carbon and oxygen signals are not discussed quantitatively, as carbon originated primarily from the conductive carbon coating applied during SEM sample preparation, while oxygen is intrinsically associated with all oxide and phosphate phases present in the materials.

In contrast, the AAC-P@HAp composite exhibits additional and prominent signals corresponding to calcium (Ca) and phosphate (P), which are absent in the AAC-P sample. The appearance of hese elements confirms the successful incorporation of a calcium-phosphate phase into the alkali-activated matrix. The simultaneous detection of Si, Al, Ca, and P indicates that the composite consists of coexisting aluminosilicate and calcium-phosphate components rather than a single homogeneous phase.

Quantitative EDX analysis further highlights the compositional details of AAC-P@HAp materials, the Ca and P contents (Ca ≈ 34 wt%, $P \approx 20$ wt%) yield a Ca/P ratio of approximately 1.7, which closely matches the stoichiometric Ca/P ratio of hydroxyapatite (1.67)[32,55,56] This agreement supports the assignment of the calcium-phosphate component in AAC-P@HAp to a hydroxyapatite-like phase. By comparison, AAC-P lacks detectable Ca and P contributions, confirming that these elements originate exclusively from the HAp modification step.

The EDX results clearly differentiate AAC-P from AAC-P@HAp in terms of elemental composition (supported by the XRF results). AAC-P is characterized by a Na–Al–Si–O framework typical of alkali-activated aluminosilicate, whereas AAC-P@HAp contains an additional calcium-phosphate component with a Ca/P ratio close to that of hydroxyapatite. These compositional features confirm successful material modification and provide a clear basis for comparing the two adsorbents in subsequent performance and stability analysis.

In all, the integrated SEM-EDX results demonstrate that HAp modification induces coordinated morphological and compositional changes, transforming AAC-P into a chemically heterogeneous composite. This balance between surface accessibility and enhanced surface chemistry underpins the potential of AAC-P@HAp for fluoride removal from aqueous systems.

3.4. Specific surface area characteristics

The textural properties of the adsorbents were evaluated using N_2 adsorption–desorption measurements. The isotherms of AAC-P and AAC-P@HAp (Fig. 3d) exhibit type IV behavior with H_3-type hysteresis loops, which are commonly associated with aggregated porous solids and slit-shaped voids formed between particle assembles.[16] This behavior confirms that alkali-activated glass matrix retains a predominantly mesoporous structure before and after hydroxyapatite incorporation.

The pristine AC-P adsorbent material exhibits a relatively high BET surface area of 187.1 $m^2\ g^{-1}$, which could be attributed to the formation of porous aluminosilicate network during alkali activation. This corresponding pore size distribution (Fig. 6d) reveals a broad mesoporous domain centered in the 5–10 nm range, consistent with the structural openness of the geopolymeric matrix.[57] In contrast, AAC-P@HAp shows a significantly reduced surface area (43.2 $m^2\ g^{-1}$), indicating a reduction in accessible surface area following incorporation of hydroxyapatite into the alkali-activated matrix.[58] The pore size distribution shows significant attenuation of mesopore volume across the entire 2–100 nm range (Fig. 6d), indicating pore filing and surface masking by calcium-phosphate domains within the composite. The reduction in total pore volume and suppression of smaller mesopores suggest structural densification and localized pore blocking within the composite.[59,60] Notably, the average pore diameter slightly increases after modification, which is consistent with preferential filling of smaller pores while larger mesopores remain partially accessible.

Despite the reduction in surface area, the BET constant (C) increases substantially from 20.2 (AAC-P) to 104.7 (AAC-P@HAp). The BET constant is related to the difference between the heat of adsorption of the first adsorbed layer and the heat of liquefaction of nitrogen. The increase in C therefore suggests stronger adsorbent–adsorbate interactions following hydroxyapatite incorporation. However, given the increased surface heterogeneity and pore-filling effects, the absolute value of C should be interpreted cautiously. In this study, it is used primarily as a comparative indicator of changes in surface energetic characteristics rather than as direct evidence of multilayer adsorption behavior.

The elevated C value is attributed to the introduction of calcium- and phosphate-containing surface functionalities, which create higher-energy adsorption sites relative to the silicate-dominated surface of AAC-P. These findings indicate that the modification does not simply alter textural parameters but fundamentally transforms surface chemistry. Consequently, the adsorption performance of AAC-P@HAp toward fluoride ions is governed more strongly by surface functional groups and specific chemical interactions than by surface area alone.[61]

3.5. FTIR analysis of surface functional groups and chemical interactions

Fourier-transform infrared (FTIR) spectroscopy was employed to investigate the surface functional groups and chemical bonding environments of AAC-P, hydroxyapatite (HAp), and the AAC-P@HAp composite (Fig. 3e). The FTIR spectrum of as-synthesized AAC-P is dominated by broad absorption bands, reflecting its predominantly amorphous alkali-activated glass structure. The broad band observed in the range of 3400–3500 cm^{-1} is attributed to O–H stretching vibrations of surface hydroxyl groups and physically adsorbed water, while the band at approximately 1640 cm^{-1} corresponds to H–O–H bending vibrations of molecular water. A strong and broad band centered around 1000–1050 cm^{-1} is assigned to the asymmetric stretching of Si–O–T (T = Si or Al) linkages, which is characteristic of aluminosilicate networks formed during alkali activation.[54] Additional low-intensity bands observed in the region of 450–550 cm^{-1} are associated with Si–O–Si and Si–O–Al bending vibrations. The AAC-P@HAp adsorbent displayed distinct phosphate bands at ~960, 1030, and 560 cm^{-1}, and carbonate peaks at ~870 and 1410–1450 cm^{-1}, confirming the incorporation of PO_4^{-3} ion in the composite materials, and partial carbonate substitution in Hap lattice·[62] These spectral changes confirm the formation of a hybrid material combining silicate and phosphate functional groups with the potential for enhanced ion exchange and fluoride sequestration.[63]

In all, the integration of hydroxyapatite into AAC-P significantly altered its physicochemical structure, transforming it from a porous, amorphous glassy matrix into a hybrid silicate-phosphate composite with increased crystallinity, enhanced chemical functionality, strong ion-binding sites. These properties make AAC-P@HAp a promising material for water defluoridation and other environmental remediation applications.

3.6. Fluoride sequestration of the as-synthesized materials

3.6.1 Effect of the adsorbent dosage. The effect of adsorbent dosage on fluoride adsorption capacity (q_e, mg g^{-1}) was evaluated to identify optimal operating conditions and assess the adsorption efficiency of the engineered composite. As shown in Fig. 5a, q_e decreased progressively with increasing adsorbent dosage, a trend characteristic of batch systems operating at fixed solute concentrations.

At low dosages, higher adsorption capacities were achieved due to efficient utilization of active sites and a stronger concentration gradient driving mass transfer. Increasing the adsorbent loading resulted in a decline in q_e, attributed to site overlap, particle aggregation, and underutilization of adsorption sites as equilibrium is approached.[64,65]

The modified adsorbent exhibited a high fluoride sequestration capacity of approximately 5.7 mg g^{-1} at an optimal dosage of 1 g, demonstrating the effectiveness of compositional and structural modification in enhancing adsorption performance. Although removal efficiencies exceeded 90% under several experimental conditions, adsorption performance is more appropriately interpreted using capacity-based metrics (mg $F^-\ g^{-1}$), particularly at high adsorbent dosages where removal efficiency may appear artificially elevated due to excess adsorbent relative to the available fluoride mass in solution. In this study, the maximum observed adsorption capacity of AAC-P@HAp was approximately **5.7** mg $F^-\ g^{-1}$ under the optimized conditions investigated. This enhanced uptake is primarily associated with the incorporation of calcium- and phosphate-

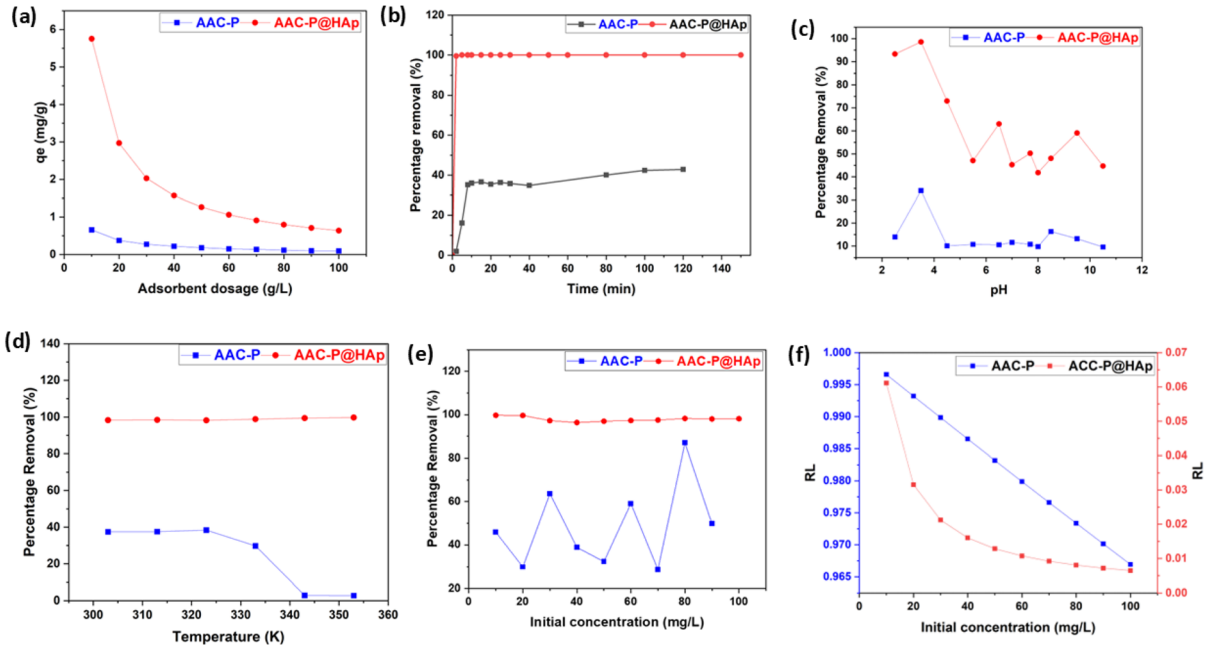

Fig. 5 (a) The effect of adsorbent dose of the interaction between adsorbent materials and fluoride ions, (b) the effect of contact time between the interaction between adsorbent materials and fluoride ions, (c) effect of pH on the sorption of fluoride ions by adsorbent materials, (d) effect of temperature on the sorption of fluoride ions by adsorbent materials, (e) the effect of the interaction between the initial concentration of fluoride ions and adsorbent materials, (f) the separation factor of fluoride ion adsorption by adsorbent materials.

rich functionalities, which facilitate fluoride removal *via* surface complexation, ion exchange, and localized precipitation. Improved surface characteristics further promote adsorption by increasing accessibility and reactivity of active sites.

These findings are consistent with earlier reports on calcium-based fluoride adsorbents[16,66] and confirm that controlled adsorbent loading is critical for maximizing adsorption efficiency. It is evident that the dosage-dependent behavior underscores the successful material design strategy adopted in this study, which significantly enhances fluoride sequestration potential under acidic (pH = 3.5) conditions.

3.6.2 The effect of contact time. The influence of contact time on fluoride sequestration is illustrated in Fig. 5b. Fluoride uptake increased rapidly during the initial stage of adsorption, followed by a short transition to equilibrium. The modified adsorbent reached adsorption equilibrium within approximately 10–20 min, after which q_e values remained nearly constant, indicating fast adsorption kinetics and efficient utilization of available active sites. The rapid initial uptake is attributed to abundant accessible surface sites and a strong driving force for mass transfer at the solid–liquid interface. As these sites became progressively occupied, adsorption approached equilibrium, resulting in a plateau in q_e. The stable adsorption profile observed at extended contact times reflects uniform site distribution and strong adsorbate–adsorbent interactions, characteristic of chemisorption-dominated processes.

The enhanced adsorption kinetics are primarily associated with hydroxyapatite incorporation, which introduces hydroxyl and phosphate functional groups capable of interacting with fluoride ions through ion exchange and surface complexation mechanisms.[67] Additionally, the modified surface architecture improves porosity and surface accessibility, facilitating rapid fluoride diffusion and binding.[68]

In all, the short equilibrium time and stable uptake behavior demonstrate the effectiveness of the material modification strategy in accelerating fluoride sequestration kinetics. These results highlight the suitability of the developed adsorbent for practical water treatment applications where rapid contaminant removal is required.

3.6.3 The effect of initial pH. The influence of initial solution pH on fluoride sequestration is presented in Fig. 5c. Fluoride removal by the developed composite remained effective over a broad pH range (2.5–10.5), with maximum uptake observed under mildly acidic conditions (pH ≈ 3.5). The enhanced performance at low pH can be attributed to favorable surface charge conditions below the point of zero charge (pH_{pzc}), which promote electrostatic attraction between fluoride ions and positively charged surface sites. In addition, ion-exchange interactions involving Ca^{2+} species and the possible formation of sparingly soluble Ca–F phases may contribute to fluoride immobilization under acidic conditions.[69]

As pH increased above neutrality, fluoride removal gradually declined, with the reduction becoming more pronounced beyond pH 7.5, due to increased competition from OH^- ions and diminished surface–fluoride interactions.[70] Despite this decline, adsorption efficiencies remained appreciable within the pH 6.5–9.5 range, which aligns with drinking water pH standards. This retention of performance over a broad pH window highlights the stabilizing role of hydroxyapatite-derived

phosphate and calcium sites, enabling effective fluoride sequestration under environmentally relevant conditions.

The observed pH dependence is attributed to changes in surface charge and fluoride speciation. At lower pH values, surface protonation enhances electrostatic attraction and facilitates ion exchange between hydroxyl groups and fluoride ions at Ca-rich sites. At higher pH, increased surface negativity leads to partial electrostatic repulsion; however, fluoride sequestration is still sustained through inner-sphere complexation and Ca–F interactions, which are less sensitive to surface charge effects.

Importantly, pH 3.5 represents an optimal condition rather than a strict operational requirement. From an application perspective, pH adjustment would not be necessary in many cases, as moderate fluoride removal can be achieved under near-neutral conditions. In addition, pH adjustment, where required, is already a common and low-cost practice in water treatment systems, particularly in decentralized or point-of-use applications.

Therefore, the results demonstrate that AAC-P@HAp remains functional across environmentally relevant pH conditions, while enhanced performance under mildly acidic conditions provides insight into the adsorption mechanism rather than a limitation for practical deployment.

3.6.4 Effect of temperature on the sorption behavior. The influence of temperature on fluoride sequestration was evaluated between 303 and 353 K at the optimized pH (Fig. 5d). Fluoride removal remained consistently high, increasing slightly from ≈98% at 303 K to nearly 100% at 353 K, indicating strong thermal stability and a mildly endothermic adsorption process. The marginal enhancement with temperature suggests improved ion diffusion and activation of chemisorption pathways, particularly those involving calcium-mediated fluoride binding.[71]

The limited variation in removal efficiency (<2%) across a 50 K temperature range indicates that the adsorption mechanism is not governed by weak physical forces but rather by stable surface interactions. Such temperature resilience is advantageous for real-world water treatment applications, especially in systems exposed to seasonal or process-related thermal fluctuations.[67]

3.6.5 Effect of initial concentrations. Fig. 5e presents the effect of initial fluoride concentration in the range of 10–100 mg L^{-1}. Fluoride removal efficiency remained consistently high at ≈98–100% throughout this concentration window, demonstrating strong affinity between fluoride ions and the available adsorption sites. The absence of a sharp decline in performance at higher concentrations indicates a high density of active sites and delayed surface saturation.

The sustained removal efficiency even at 100 mg L^{-1} suggests that adsorption proceeds *via* robust chemisorption and ion-exchange mechanisms rather than weak physisorption. Similar concentration-independent trends have been reported for calcium- and phosphate-modified adsorbents, where fluoride uptake is stabilized by surface complexation and precipitation-assisted mechanisms.[16,72,73] These results confirm the material's suitability for treating waters with both moderate and elevated fluoride levels.

3.6.6 The kinetic behavior of fluoride ions sorption. The adsorption kinetics of fluoride onto AAC-P and AAC-P@HAp were evaluated using multiple kinetic models to elucidate the dominant rate-controlling steps and adsorption stages (Table 7). The comparative analysis reveals a fundamental shift in adsorption behavior upon hydroxyapatite incorporation, confirming a transition from weakly controlled adsorption on AAC-P to rapid, multi-stage, and chemically driven adsorption on AAC-P@HAp.

For AAC-P@HAp, the pseudo-first-order (PFO) model provides an excellent fit to the experimental data ($R^2 = 0.99972$), with a substantially higher apparent rate constant ($k_1 = 2.65\ min^{-1}$) and equilibrium adsorption capacity ($q_e = 3.27$ mg g^{-1}) compared to AAC-P. This indicates that fluoride uptake on AAC-P@HAp is initially rapid and dominated by surface-controlled processes, consistent with strong electrostatic attraction and immediate interaction with readily available active sites.

In contrast, the pseudo-second-order (PSO) model exhibits lower correlation coefficients ($R^2 \approx 0.85$ for both materials), suggesting that although chemisorption contributes to fluoride sequestration, adsorption does not proceed *via* a single rate-limiting chemical step. Nevertheless, the extremely high initial adsorption rate ($h = 7242.6$ mg g^{-1} min^{-1}) observed for AAC-P@HAp highlights the high reactivity of calcium-phosphate sites and confirms the rapid establishment of strong fluoride-surface interactions.

The intraparticle diffusivity parameters further support a multi-stage adsorption mechanism. The markedly high diffusion constant for AAC-P@HAp ($k = 32.57$ mg g^{-1} $min^{-1/2}$) compared to AAC-P ($k = 0.0209$ mg g^{-1} $min^{-1/2}$) indicates efficient internal mass transport of fluoride ions within the composite structure. However, the moderate correlation coefficient ($R^2 = 0.8545$) suggests that intraparticle diffusion is not the sole rate-controlling step, implying the simultaneous involvement of surface adsorption and chemical interactions.

Additional insight is provided by the Elovich model, which shows a strong fit for AAC-P@HAp ($R^2 = 0.9912$). The elevated Elovich constant ($A = 6.01$ mg g^{-1} min^{-1}) reflects a high density of energetically heterogeneous active sites, while the B parameter indicates increasing activation energy as adsorption progresses. This behavior is characteristic of systems dominated by chemisorption on heterogeneous surfaces.

The Avrami kinetic model provides the most comprehensive description of fluoride adsorption onto AAC-P@HAp, yielding an excellent correlation ($R^2 = 0.99972$) and an Avrami exponent $n = 1.68$. The non-integer Avrami exponent confirms that adsorption proceeds through multiple overlapping stages involving progressive surface growth and site activation rather than simple monolayer saturation. This behavior is consistent with fluoride uptake driven by hydroxyl-fluoride ion exchange, inner-sphere complexation, and gradual structural incorporation into hydroxyapatite domains.

In effect, the kinetic parameters collectively indicate that fluoride sequestration onto AAC-P@HAp occurs through three

Table 7 Kinetic model parameters of the adsorbent materials

Kinetic models		AAC-P	AAC-P@HAp
Pseudo first order	k_1 (min^{-1})	0.119 975	2.645 153
	q_e (mg g^{-1})	0.325 997	3.268 122
	R^2	0.871 709	0.99972
Pseudo second order	k_2 (g mg^{-1} min^{-1})	0.420 126	32.56922
	h(mg g^{-1} min^{-1})	0.03278	7242.61
	q_e (mg g^{-1})	0.364 496	3.269 258
	R^2	0.855 643	0.854 543
Intra particle diffusivity (Weber–Morris Model)	k(g mg^{-1} $min^{-1/2}$)	0.020857	32.56922
	C(mg g^{-1} min^{-1})	0.144 836	3.269 258
	R^2	0.530 981	0.854 543
Elovich	A (mg g^{-1} min^{-1})	0.155 316	6.00723
	B(g mg^{-1})	15.41307	8.88400
	R^2	0.748 396	0.99120
Avrami	q_e(mg g^{-1})	0.325 887	3.268 122
	k_{Av}(1/min)	0.385 427	1.573 496
	n_{Av}	0.311 271	1.681 067
	R^2	0.871 709	0.99972

sequential stages: (i) rapid surface adsorption controlled by electrostatic attraction and readily accessible Ca-rich sites, (ii) diffusion-assisted penetration into the composite structure, and (iii) chemisorption-controlled stabilization through fluorin de incorporation into calcium-phosphate domains. This multi-stage kinetic behavior confirms that hydroxyapatite integration effectively transforms AAC-P into a fast-acting and mechanistically robust fluoride adsorbent, directly fulfilling the study objective of achieving rapid and stable fluoride immobilization.

3.6.7 Adsorption isotherms of the materials. The equilibrium adsorption behavior of fluoride on AAC-P and AAC-P@HAp was evaluated using the Langmuir, Freundlich, Temkin and Dubinin–Radushkevich (D–R) models (Fig. 5f and Table 8). These models provide complementary insights into surface heterogeneity, adsorption energetics, and binding mechanisms.

The Freundlich model describes adsorption on energetically heterogeneous surfaces with multilayer uptake. Both adsorbents showed good fits to the Freundlich equation, with AAC-P (R^2 = 0.9326) and AAC-P@HAp (R^2 = 0.8746), indicating that fluoride adsorption occurs on surfaces with a distribution of adsorption energies rather than uniform sites.

The Freundlich n values for AAC-P (0.595) and AAC-P@HAp (0.475) are both <1, indicating favorable but cooperative adsorption, where surface sites become increasingly reactive as adsorption proceeds typical for chemisorption-dominated heterogeneous materials. The much higher K_f value for AAC-P@HAp (0.330 mg g^{-1}) compared with AAC-P (0.000536 mg g^{-1}) demonstrates a substantially greater surface affinity, directly attributable to the introduction of Ca-PO_4 functional groups from hydroxyapatite.

The Langmuir model, which assumes monolayer adsorption on uniform active sites, fits AAC-P@HAp significantly better as compared to AAC-P (R^2 = 0.8733 *vs.* 0.7714). The maximum monolayer capacity (A_s) increases dramatically from 0.240 mg g^{-1} (AAC-P) to 4.612 mg g^{-1} (AAC-P@HAp), confirming that hydroxyapatite introduces high-affinity binding sites capable of strong fluoride capture.

The Langmuir separation factor (RL), calculated from Langmuir constants and plotted in Fig. 5b, provides a rigorous assessment of adsorption favorability. In the case of AAC-P, RL decreases slightly from ~0.997 to ~0.967 as fluoride concentration increases, indicating weak but favorable adsorption. For AAC-P@HAp, RL drops sharply from ~0.06 at low concentrations to below 0.01 at higher concentrations. Since 0 < RL < 1 indicates favorable adsorption, and RL → 0, which implies a highly favorable or quasi-irreversible adsorption, AAC-P@HAp clearly exhibits strong, highly favorable fluoride binding, consistent with surface complexation and precipitation mechanisms rather than simple physical sorption.

The Temkin model shows poorer fits (R^2 < 0.70), indicating that heat of adsorption does not decrease linearly with coverage. However, AAC-P@HAp exhibits a much higher Temkin A constant, reflecting stronger adsorbent–adsorbate interactions.

The Dubinin–Radushkevich model also yields moderate fits, but the very high theoretical qm for AAC-P@HAp

Table 8 Isotherms model parameters for the removal of fluoride ions from aqueous solution by adsorbent materials

		Materials	
Isotherm models		AAC-P	AAC-P@Hap
Freundlich	N	0.595 052	0.47533
	K_f (mg g^{-1})	0.000536	0.330 344
	R^2	0.932 553	0.874 578
Langmuir	b(L mg^{-1})	0.00034	1.53532
	A_s (mg g^{-1})	0.239 787	4.61236
	R^2	0.77140	0.87330
Temkin	A (L mg^{-1})	0.112 015	46.35243
	B (Kcal mol^{-1})	18 606.7	3723.70
	dQ (J mg^{-1})	13 462.69	12 818.3
	R^2	0.696 150	0.587 487
Dubinin–Radushkevich	β (mol^2 kJ^{-2})	2×10^5	2×10^6
	q_m (mmol g^{-1})	3.824 776	66.93
	R^2	0.5778	0.7328

Table 9 Thermodynamic parameters of the uptake of fluoride ions by adsorbent materials

Materials	$\Delta H°$ (kJ mol^{-1})	$\Delta S°$ (J mol^{-1}.K)	$\Delta G°$(kJ mol^{-1}) 303 K	313 K	323 K	333 K	343K	353K
AAC-P	+45.28	+172.94	−7.45	−8.99	−9.95	−11.57	−15.30	−15.54
AAC-P@HAp	+31.33	+166.52	−20.04	−20.99	−21.27	−23.05	−25.73	−28.83

(66.93 mmol g^{-1}) suggests that fluoride sequestration is not limited to simple micropore filling, but involves chemical interaction with Ca^{2+} and PO_4^{3-} sites, consistent with fluorapatite formation.

3.7. Thermodynamic characteristics of fluoride sorption

The thermodynamic parameters (Table 9) further confirm the fundamental differences between AAC-P and AAC-P@HAp. The positive enthalpy ($\Delta H°$) values of +45.28 kJ mol^{-1} (AAC-P) and +31.33 kJ mol^{-1} (AAC-P@HAp) indicate that fluoride adsorption is endothermic, meaning higher temperatures promote stronger uptake. The magnitude of $\Delta H°$ for AAC-P@HAp falls in the chemisorption range, whereas AAC-P lies closer to weak chemisorption or strong physisorption.

Gibbs free energy values ($\Delta G° = -7.47$-15.54 kJ mol^{-1} for AAC-P, −20.04 to −28.83 kJ mol^{-1} for AAC-P@HAp) are negative across all temperatures, confirming spontaneous adsorption. The larger negative $\Delta G°$ values and higher ln K_c for AAC-P@HAp reflect stronger fluoride binding and greater thermodynamic favorability. While AAC-P mainly exhibits physisorption, AAC-P@HAp shows characteristics of chemisorption, attributed to Ca^{2+}-F^- interactions from hydroxyapatite[71]

In all, AAC-P@HAp demonstrates enhanced adsorption performance, stronger binding energy, and higher thermal stability, making it a more effective adsorbent for anion removal under variable temperature conditions. The positive entropy change ($\Delta S°$) reflects increased disorder at the solid–liquid interface, caused by fluoride dehydration and restructuring of surface sites during binding.

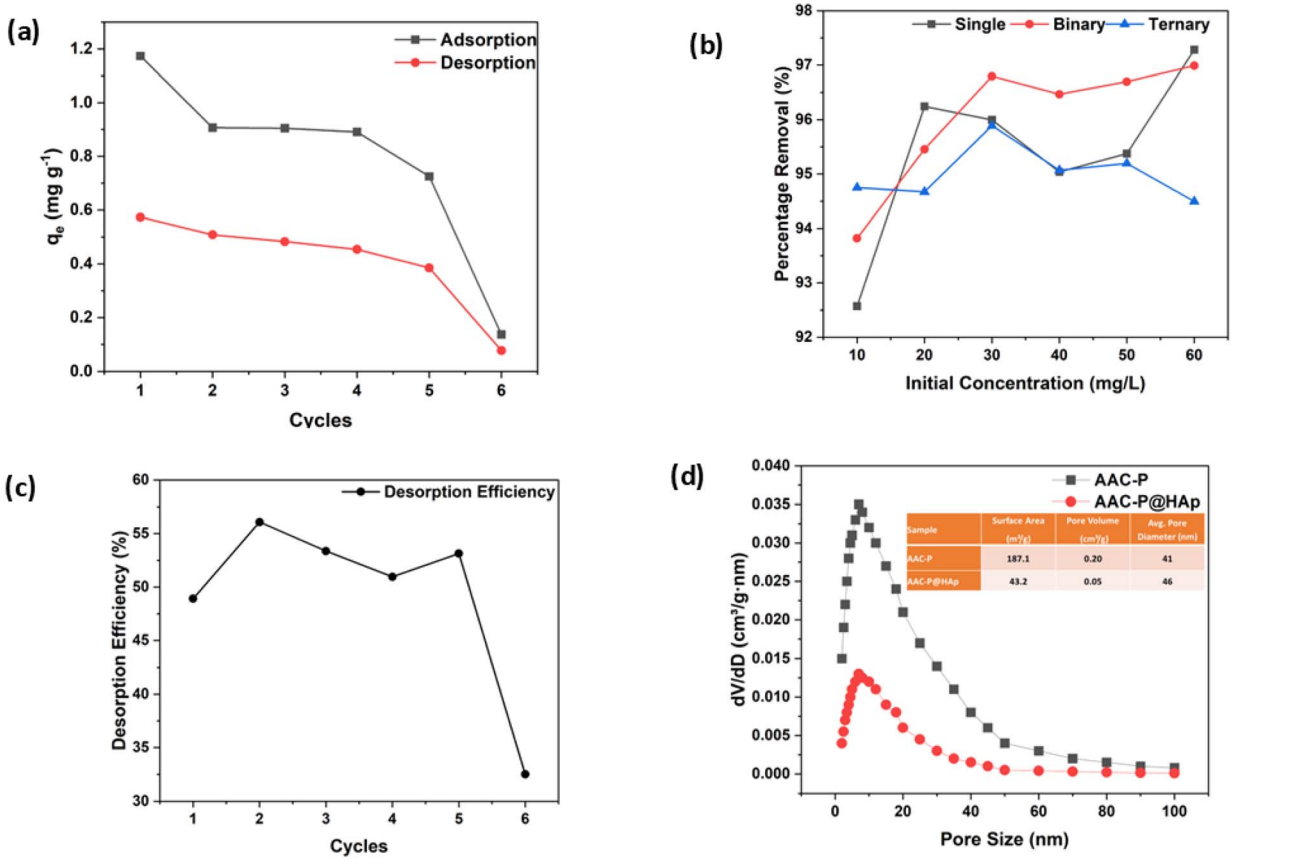

Fig. 6 (a) Adsorption–desorption capacity over successive cycles (reusability), (b) influence of co-existing ions on fluoride removal performance of AAC-P@HAp, (c) desorption efficiency during regeneration, (d) BJH pore size distribution (desorption branch) of AAC-P and AAC-P@HAp from N_2 adsorption–desorption isotherms at 77 K.

The negative Gibbs free energy ($\Delta G°$) values confirm spontaneous adsorption for both materials, but AAC-P@HAp exhibits far more negative values (−20 to −28.8 kJ mol^{-1}) than AAC-P (−7.5 to −15.5 kJ mol^{-1}), demonstrating much stronger thermodynamic driving force and more stable fluoride binding.

3.8. Effect of ionic strength

Real wastewater contains diverse inorganic salts that may interfere with pollutant adsorption (Wang *et al.*, 2024). To evaluate the robustness of AAC-P@HAp, the impact of sodium cyanide (NaCN) and potassium sulphate (K_2SO_4) at concentrations of 10–60 mg L^{-1} was assessed in single, binary and ternary systems using 1 g L^{-1} of the adsorbent. As shown in Fig. 6c, AAC-P@HAp consistently achieved high fluoride removal efficiencies (>92%) across all systems, with the highest performance in single-ion systems (>97%) and slightly declines in binary (95–97%) and ternary (92–95%) systems.

The high resilience to ionic interference can be attributed to several factors. First, electrostatic neutralization by Na^+ and K+ions likely reduce repulsion between fluoride and the adsorbent surface, enhancing fluoride access, especially under low ionic strength. Second, structural activation of the composite by surrounding ions may lead to slight swelling or reorganization of surface functional groups, improving pore accessibility and diffusion.[74] Third, although competitive ion-surface interaction may occur, the strong affinity between fluoride and the calcium/phosphate sites in hydroxyapatite dominates, maintaining effective adsorption.

These results confirm AAC-P@HAp as a robust and efficient fluoride adsorbent, retaining high performance even in the presence of interfering ions. Its stability and high selectivity under multicomponent conditions support its practical use in complex water metrices, aligning with findings from similar bio-composite systems.[75,76]

3.9. Response surface methodology

The Box–Behnken model was statistically significant ($p < 0.05$) with a non-significant lack-of-fit ($p > 0.05$), which indicates the acceptable adequacy within the explored design space. Among the tested variables, the solution pH exerted the dominant effect on fluoride removal ($p << 0.05$), while adsorbent dose and temperature showed comparatively weak effects. Detailed response-surface, contour and cube-plot visualizations are therefore provided in the supplementary information (Fig. S1a–e) to avoid overinterpretation of small interaction contributions. The predicted removal efficiency across the investigated domain varied narrowly (83–87%) consistent with modest experimental response range.

3.10. Regeneration of the AAC-P@HAp-adsorbent material

The regeneration behavior of AAC-P@HAp was systematically evaluated over six consecutive adsorption–desorption cycles to assess its operational durability and the nature of fluoride uptake (Fig. 7a). In the first cycle, the adsorbent retained 93.80% fluoride removal efficiency, indicating that a fraction of the initially adsorbed fluoride was reversibly bound and could be partially released during alkaline regeneration. This initial reversibility suggests that the contribution of weak surface interactions and electrostatic attraction, particularly at protonated surface sites and accessible aluminosilicate domains.

With increasing regeneration cycles, a pronounced and progressive decline in fluoride removal efficiency was observed. The removal efficiency decreased to approximately 72% by the third cycle and further declined to 10.95% by the sixth cycle,

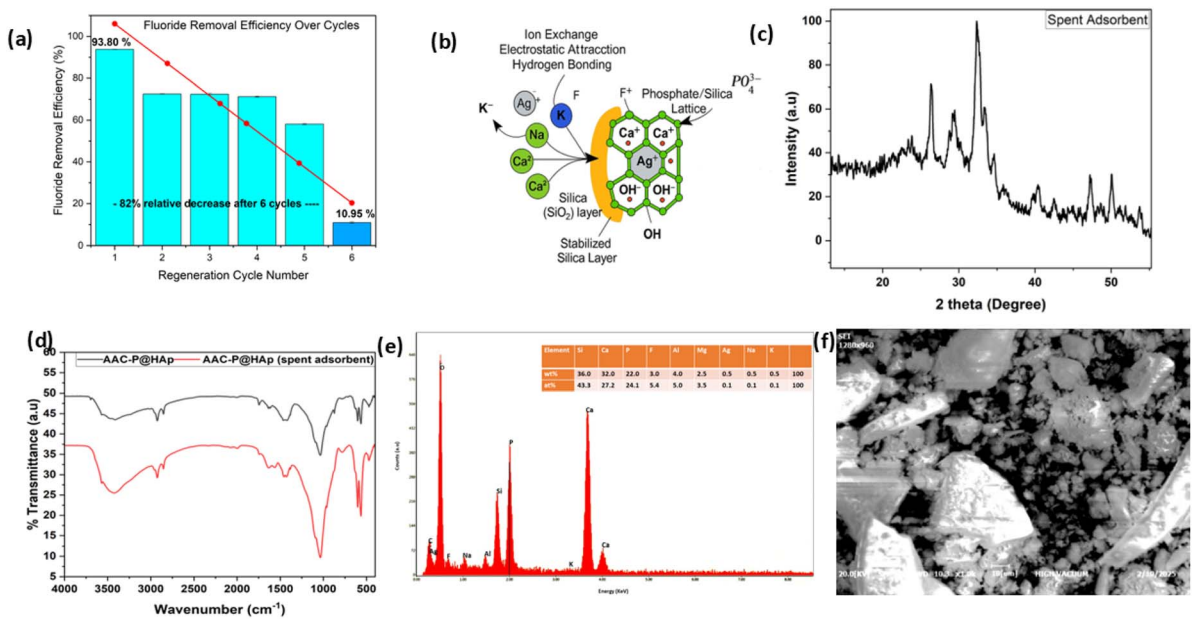

Fig. 7 (a) Regeneration cycle chart of AAC-P@HAp-fluoride ions interaction, (b) schematic illustration of the adsorption mechanism of AAC-P@HAp, (c) XRD diffraction pattern of spent AAC-P@HAp adsorbent material, (d) FTIR spectrum of raw and spent AAC-P@HAp adsorbent material, (e) EDX peaks of the spent AAC-P@HAp adsorbent material, (f) SEM image of the spent AAC-P@HAp adsorbent material.

which indicate the substantial loss of available reactive sites. In addition, this behavior demonstrates that fluoride removal is not governed by reversible physisorption alone. Quantitative adsorption–desorption mass balance analysis (Fig. 6b and c) shows that only approximately 32.50–56.09% of the adsorbed fluoride could be desorbed per cycle, confirming that a significant fraction of fluoride sequestration is irreversible.

Importantly, the observed performance loss is not attributed to physical degradation of the adsorbent, but rather to progressive chemical transformation and depletion of active sites. This interpretation is strongly supported by complementary structural and surface analysis. The point of zero charge (pH_{pzc}) shifted from ~10.56 for fresh AAC-P@HAp to ~7.00 after fluoride sequestration, reflecting substantial alteration of surface chemistry due to fluoride incorporation. This shift confirms that fluoride ions are not merely electrostatically bound but are chemically immobilized through ion exchange and inner-sphere complexation, replacing surface –OH and phosphate groups.

SEM micrographs of the spent adsorbent reveal surface aggregation and particle coalescence, consistent with the formation of new surface phases (Fig. 7f). Correspondingly, EDX spectra confirm the presence of fluoride along with Ca and P, indicating the formation of Ca–F and Ca–P–F species (Fig. 7e). FTIR spectra further support this observation through the attenuation of –OH stretching vibrations and modification of phosphate-related bands (Fig. 7d), which suggest the transformation of hydroxyapatite domains into fluorapatite-like structures. These findings are corroborated by XRD patterns (Fig. 7c), which show the emergence of new diffraction features and slight peak shifts attributable to fluoride-containing calcium phosphate phases, while maintaining overall structural integrity.

Taken together, these results demonstrate that fluoride removal by AAC-P@HAp is govern by a combination of initial reversible adsorption and dominant irreversible chemisorption/phase transformation at later stages. Although this behavior limits log-term renderability, it confers a high degree of fluoride fixation and chemical stability, which is advantageous for preventing secondary fluoride release.

In all, AAC-P@HAp exhibits effective short-term reusability (up to three cycles) followed by strong and permanent fluoride immobilization. Accordingly, the material is best described as a reactive fluoride sequestration medium with partial early-cycle renderability, suitable for application where secure immobilization is prioritized over extensive reuse, with periodic replacement or chemical rejuvenation as a practical operation strategy.

3.11. Fluoride sequestration mechanism of AAC-P@HAp

Fluoride sequestration onto AAC-P@HAp proceeds through synergistic interactions between the alkali-activated aluminosilicate framework and embedded hydroxyapatite (HAp) domains. The mechanism is elucidated using pH-dependent adsorption behavior, surface charge analysis (pH_{pzc}), spectroscopic and diffraction evidence (FTIR and XRD), elemental distribution (SEM-EDX), post-adsorption calcium analysis (ICP-OES), and regeneration performance. Collectively, these results demonstrate that fluoride removal is dominated by chemisorption, with electrostatic attraction governing only the initial uptake stage.

It is acknowledged that fluoride sequestration onto AAC-P@HAp is dominated by the hydroxyapatite phase, consistent with extensive literature reports on HAp-based fluouride immobilization.[16,77,78]

Although fluoride sequestration is primarily governed by the hydroxyapatite phase, the AAC-P matrix performs several important structural and functional roles. First, the alkali-activated aluminosilicate network provides a mechanically stable support that immobilizes hydroxyapatite particles and prevents aggregation.[79,80] Second, the porous AAC-P framework promotes dispersion of calcium-phosphate domains, thereby increasing the accessibility of reactive Ca-sites compared with bulk HAp powders.[81] Third, the composite architecture improves material handling and deployability, since hydroxyapatite powders alone often exhibit poor mechanical stability and are difficult to recover from treated water.[58] The integration of hydroxyapatite within the AAC-P matrix therefore transforms the material from a fine particulate sorbent into a structurally robust composite suitable for practical water treatment applications. The present study does not aim to demonstrate enhanced intrinsic adsorption capacity relative to standalone hydroxyapatite. Instead, the contribution of AAC-P lies in providing a chemically stable and waste-derived support matrix that enables dispersion and immobilization of hydroxyapatite domains, thereby improving material handling, structural integrity and potential deployability. By integrating hydroxyapatite into an alkali-activated waste glass framework, the applicability of waste-glass-based materials are extended from predominantly cationic adsorption[21–26] towards anionic contaminant removal, while maintaining sustainability and reducing reliance on standalone fine HAp powders.

The fresh AAC-P@HAp composite exhibits a high pH_{pzc} ($\approx$10.56), indicating a positively charged surface under acidic to near-neutral conditions. At solution pH values below the pH_{pzc}, protonation of surface hydroxyl, silanol, and phosphate groups enhances electrostatic attraction of fluoride ions, enabling rapid initial adsorption (eqn (8) and (9)):

$$\equiv MOH + H^+ \rightarrow \equiv MOH_2^+ \quad (8)$$

$$\equiv MOH_2^+ + F^- \rightarrow \equiv MOH_2^+ \cdots F^- \quad (9)$$

where *M* represents Ca-, Si-, or Al-associated surface sites. This initial interaction explains the high adsorption rate and the relatively high regeneration efficiency observed during the first cycle.

However, following fluoride uptake, the pH_{pzc} shifts markedly to 7.00, indicating substantial alteration of surface chemistry. This shift confirms that fluoride is not merely electrostatically bound but is progressively incorporated through chemical binding process. The concomitant decline in regeneration efficiency over successive cycles further supports the increasing contribution of irreversible chemisorptive interactions.

FTIR spectra provide direct evidence for this transition (Fig. 7d). After adsorption, attenuation and slight shifts of O–H stretching bands indicate consumption or modification of surface hydroxyl groups, while modifications in phosphate-related PO_4^{3-} vibrations reflect changes in the coordination environment of HAp phase. These changes are consistent with hydroxyl-fluoride ion exchange within hydroxyapatite domains as indicated in reaction 10:

$$Ca_{10}(PO_4)_6(OH)_2 + 2F^- \rightarrow Ca_{10}(PO_4)_6F_2 + 2OH^- \quad (10)$$

The XRD patterns of the spent adsorbent (Fig. 7c) further corroborate this mechanism. While no crystalline CaF_2 phase is detected, subtle peak shifts and changes in HAp reflection intensities are observed after adsorption, indicating lattice-level fluoride incorporation and partial transformation of hydroxyapatite into fluorapatite-like structures rather than bulk precipitation.

SEM-EDX analysis (Fig. 7e and f) of the spent adsorbent provides direct compositional evidence for calcium-mediated fluoride immobilization at hydroxyapatite domains. Elemental point spectra reveal clear co-localization of fluoride with calcium and phosphorus, confirming that fluoride uptake occurs preferentially at Ca–P rich regions rather than uniformly across the aluminosilicate matrix. This spatial association supports inner-sphere interactions between luoride ions and calcium sites within hydroxyapatite-derived phases, as represented by reaction 11:

$$\equiv Ca^{2+} + F^- \rightarrow \equiv Ca–F \quad (11)$$

Quantitative EDX analysis further substantiates this mechanism. For the spent AAC-P@HAp, the calcium and phosphorus contents are approximately Ca $\approx$ 32 wt% and $P \approx$ 22 wt%, corresponding to a Ca/P atomic ratio of 1.45. This value is lower than the stoichiometric Ca/P ratio of crystalline hydroxyapatite (1.67), but remains within the range reported for calcium-deficient or partially transformed apatite phases. The observed decrease in Ca/P after fluoride sequestration therefore indicates partial calcium consumption or redistribution, consistent with fluoride immobilization through hydroxyl-fluoride exchange and lattice-level incorporation rather than simple physical adsorption.

Additional insight is provided by the Ca/F ratio derived from EDX spectra of the spent adsorbent. With Ca $\approx$ 32 wt% and $F \approx$ 3 wt%, the calculated Ca/F ratio of approximately 10–11 is substantially higher than the stoichiometric ratio expected for bulk calcium fluoride (CaF_2). This elevated Ca/F ratio indicates that fluoride sequestration does not proceed through uncontrolled CaF_2 precipitation. Instead, it supports a mechanism dominated by surface-limited ion exchange and complexation processes, including (i) formation of Ca–F surface complexes and (ii) partial substitution of hydroxyl groups in hydroxyapatite to yield fluorapatite-like domains:

$$Ca_{10}(PO_4)_6(OH)_2+2F^- \rightarrow Ca_{10}(PO_4)_6F_2 + 2OH^- \quad (12)$$

The absence of distinct CaF_2 reflections in the XRD patterns of the spent adsorbent further corroborates this interpretation, confirming that fluoride is immobilized predominantly through surface-mediated and lattice-substitution mechanisms rather than bulk precipitation. Taken together, the SEM-EDX compositional ratios, spatial co-localization of Ca, P, and F, and complementary spectroscopic and diffraction evidence collectively demonstrate that fluoride sequestration in AAC-P@HAp is governed by chemically controlled calcium–phosphate interactions, leading to stable and largely irreversible immobilization.

Complementary ICP-OES analysis reveals a post-adsorption calcium concentration of 1043.17 mg L^{-1}, indicating partial release of Ca^{2+} during fluoride uptake. This leaching is attributed to localized interfacial dissolution accompanying hydroxyl-fluoride exchange within HAp domains.[82] Importantly, the absence of CaF_2 reflections in XRD patterns confirms that fluoride removal is governed by surface-mediated dissolution-reincorporation and lattice substitution processes rather than uncontrolled precipitation in solution.

The alkali-activated glass matrix provides a chemically stable and porous scaffold that disperses HAp domains and enhances mass transfer. Surface silanol groups may contribute secondary adsorption through weak, reversible outer–sphere interactions or hydrogen bonding (reaction 13):

$$\equiv Si–OH + F^- \rightarrow \equiv Si–OH\cdots F^- \quad (13)$$

However, these interactions are considered minor relative to calcium-mediated chemisorption.

Finally, fluoride sequestration by AAC-P@HAp follows a multi-stage mechanism involving: (i) rapid electrostatic attraction at protonated surface sites, (ii) hydroxyl-fluoride ion exchange within hydroxyapatite, (iii) inner-sphere complexation with Ca^{2+} centers, and (iv) partial lattice incorporation into fluorapatite-like structures accompanied by limited calcium dissolution and reincorporation. The dominance of these irreversible chemisorptive processes explains both the high fluoride immobilization efficiency and the progressive decline in regeneration performance, confirming AAC-P@HAp as a robust material for permanent fluoride stabilization rather than repeated reversible adsorption.

3.11.1 Benchmarking AAC-P@HAp against CaO-rich AAC_P system (AAC-P@Ca). A direct comparison between AAC-P@HAp and previously reported CaO-rich AAC-P system highlights a clear trade-off between fluoride uptake capacity and chemical stability (SI Table S1). AAC-P@HAp exhibits a high pH_{pzc} (10.56), ensuring a positively charge surface under acidic to near neutral conditions that favours electrostatic attraction of fluoride ions. However, incorporation of hydroxyapatite leads to a reduced BET surface (43.2 $m^2 g^{-1}$) due to partial pore filling and surface masking by calcium-phosphate crystallites. Unlike CaO-rich composite (AAC-P@Ca)[16] where fluoride uptake is strongly driven by highly alkaline conditions ($pH_{pzc} = 12.6$) and rapid calcium dissolution, fluoride removal by AAC-P@HAp proceeds predominantly *via* hydroxyl-fluoride exchange and inner-sphere complexation within hydroxyapatite domains. This mechanism is supported by ICP-OES analysis, which reveals partial Ca^{2+} release (1043.17 mg L^{-1}) during adsorption, attributed to localized interfacial dissolution accompanying

Table 10 Comparison of the adsorption of fluoride ions by different adsorbents

Adsorbent	Removal efficiency (%)	Fluoride concentration (mg L^{-1})	Solution pH	Temperature (°C)	Reference
AAC-P@HAp	**>98 (5.47 mg g^{-1})**	**10–100**	**3.5**	**60**	**This study**
Bivalve shell	97.26 (27.31 mg g^{-1})	3	5.5	—	83
MOF-801	92.3 (19.42 mg g^{-1})	5–25	—	—	84
Zeolite	90.0 (0.47 mg g^{-1})	18.3	—	—	85
Untreated pumice	65.4 (11.765 mg g^{-1})	5–10	6	10–50	86
Magnesium-doped nano ferrihydrite	66–91 (64 mg g^{-1})	10–15	1–10	20–45	87

fluoride incorporation rather than bulk precipitation. Consequently, AAC-P@HAp exhibits lower gravimetric fluoride uptake but significantly enhanced chemical stabilization of fluoride through fluorapatite-like incorporation, reducing uncontrolled calcium mobility and improving material integrity. This distinction demonstrates that AAC-P@HAp is not a capacity-optimized analogue of CaO-rich AAC-P, but rather a stabilization-oriented composite designed for secure fluoride immobilization and practical deployment.

3.11.2 Comparison of enhanced AAC-P@HAp with other adsorbent materials reported in the literature. The fluoride removal performance of AAC-P@HAp was benchmarked against representative adsorbents reported in the literature, as summarized in Table 10. Under optimized batch conditions (fluoride concentration 10–100 mg L^{-1}, pH 3.5, 60 °C), AAC-P@HAp achieved fluoride removal efficiencies above 98%, which places it within the performance range of several advanced fluoride sorbents.

For example, bivalve shell-based materials reported by Hahemkhani *et al.*[83] reached 97.26% removal at a lower fluoride concentration (3 mg L^{-1}), while MOF-801 exhibited approximately 92.3% removal in the 5–25 mg L^{-1} range.[84] Similarly, zeolites and pumice-based materials typically show lower efficiencies, particularly at higher fluoride concentrations, with reported values between 65 and 90%.[85,86] Metal-based adsorbents such as magnesium-doped ferrihydrite can reach higher efficiencies (up to ~90%), but often require strongly acidic conditions (pH 1–3) to operate effectively.[88]

Although AAC-P@HAp requires mildly acidic conditions (pH ≈ 3.5) and moderate heating (60 °C) to achieve near-complete fluoride removal, these conditions are less extreme than those reported for some metal oxide or ferrihydrite-based adsorbents. In addition, its ability to operate across a relatively wide fluoride concentration range (10–100 mg L^{-1}) suggest that the potential applicability for both drinking water and industrial effluents, where fluoride levels can vary significantly.

From a materials perspective, the competitive performance of AAC-P@HAp can be attributed to the combined contributions of the alkali-activated aluminosilicate matrix and hydroxyapatite. The former (AAC-P) provides a porous, ion-accessible framework, while the latter (HAp) introduces calcium- and phosphate-rich surface sites with known affinity for fluoride. This synergistic structure allows AAC-P@HAp to reach adsorption efficiencies comparable to those of more complex materials such as MOFs, while being synthesized from low-cost waste-derived precursors.

In effect, when compared with reported adsorbents, AAC-P@HAp demonstrates promising fluoride removal capability under controlled laboratory conditions. With further optimization of operating pH, regeneration strategy, and reactor configuration (*e.g.*, fixed-bed operation), this composite has potential for application in practical water and wastewater treatment systems, particularly in regions affected by fluoride contamination.

4. Conclusion

This study demonstrates that the waste-derived alkali-activated glass-hydroxyapatite composite (AAC-P@HAp) is an effective and sustainable adsorbent for fluoride removal from aqueous systems. Fluoride sequestration is dominated by chemisorptive mechanisms, initiated by electrostatic attraction at protonated surface sites and followed by hydroxyl-fluoride ion exchange and inner-sphere complexation within hydroxyapatite domains. These interactions promote partial lattice incorporation of fluoride into fluorapatite-like structures, resulting in strong and stable immobilization.

Comprehensive characterization using FTIR, XRD, SEM-EDX, surface charge analysis, and ICP-OES collectively confirm chemical incorporation of fluoride rather than weak physical adsorption or uncontrolled bulk precipitation. The observed Ca^{2+} release during adsorption is attributed to localized interfacial dissolution accompanying hydroxyl-fluoride exchange within hydroxyapatite domains, followed by fluoride reincorporation into calcium-phosphate phase, without compromising structural integrity.

Regeneration studies reveal high initial reusability, followed by a progressive decline in performance due to irreversible chemisorption and depletion of active exchangeable sites. While this limits long-term regeneration, it highlights the material's strong fluoride fixation capacity and suitability for application prioritizing secure immobilization over repeated reuse.

While fluoride sequestration in AAC-P@HAp is governed by established hydroxyapatite-based mechanisms, the key contribution of this work lies in demonstrating a fully waste-derived composite strategy that enhances the applicability and functional versatility of alkali-activated glass for anionic pollutant removal. By integrating hydroxyapatite into a chemically robust

alkali-activated glass matrix derived from waste glass, agricultural ash, and eggshells, this study extends the use of waste glass-based materials beyond predominantly cationic adsorption towards controlled anionic fluoride immobilization. This approach aligns with circular economy principles and supports the development of sustainable, decentralized and long-term defluoridation solutions.

Author contributions

Bennet Edem Akorley: writing – review & editing, writing – original draft, visualization, validation, methodology, formal analysis, data curation, conceptualization. Ohene B. Apea: writing – review & editing, writing – original draft, visualization, validation, supervision, resources, project administration, formal analysis, conceptualization. Girum Ayalneh Tiruye: writing – review & editing, writing – original draft, validation, supervision, resources, project administration, funding acquisition, formal analysis, conceptualization.

Conflicts of interest

There are no competing interests of financial or personal nature.

Data availability

The data generated during the research are with the corresponding author and may be made available upon request.

Supplementary information (SI): additional data supporting this study, including a comparative assessment of CaO-rich and hydroxyapatite-modified composites (Table S1), detailed statistical analysis of adsorption parameters using Box–Behnken design (Tables S2–S4), and response surface modelling results; figures illustrating interaction effects, optimization plots, and model validation, as well as extended discussion of adsorption behaviour and process parameter influence. See DOI: https://doi.org/10.1039/d6ra00457a.

Acknowledgements

Funding: This work was supported by The European Commission/European union in collaboration with African Union under Intra-Africa Academic Mobility scheme for the ESIMSAD project [grant number 624175].

References

1 S. Ahmad, R. Singh, T. Arfin and K. Neeti, Fluoride contamination, consequences and removal techniques in water: a review, *Environ. Sci.: Adv.*, 2022, 620–661, DOI: 10.1039/d1va00039j.

2 H. Kabir, A. K. Gupta and S. Tripathy, Fluoride and human health: Systematic appraisal of sources, exposures, metabolism, and toxicity, *Crit. Rev. Environ. Sci. Technol.*, 2020, **50**(11), 1116–1193, DOI: 10.1080/10643389.2019.1647028.

3 Y. S. Solanki, M. Agarwal, A. B. Gupta, S. Gupta and P. Shukla, Fluoride occurrences, health problems, detection, and remediation methods for drinking water: A comprehensive review, *Sci. Total Environ.*, 2022, **807**(Pt 1), 150601, DOI: 10.1016/j.scitotenv.2021.150601.

4 J. K. Efavi, A. Yaya, S. Adeborna and J. Fobil, Development and Comparative Analysis of Aluminosilicate Based Ceramic Filters for Ground Water Defluoridation, *Adv. Meat Res. v*, 2014, **936**, 822–828, DOI: 10.4028/www.scientific.net/amr.936.822.

5 T. Onipe, J. N. Edokpayi and J. O. Odiyo, A review on the potential sources and health implications of fluoride in groundwater of Sub-Saharan Africa, *J. Environ. Sci. Health Part A*, 2020, 1078–1093, DOI: 10.1080/10934529.2020.1770516.

6 K. K. Tiwari, R. Raghav and R. Pandey, Recent advancements in fluoride impact on human health: A critical review, *Environ. Sustain. Indic.*, 2023, DOI: 10.1016/j.indic.2023.100305.

7 R. Chaudhuri, S. Sahoo, A. Desarkar and S. Hazra. Fluoride Contamination in Groundwater- A Review, In. *Environmental Science and Engineering*, ed. Shit P. K., Dutta D., Das T. K., Das S., Bhunia G. S. and Das P., Springer International Publishing, Cham, 2024. pp, 331–354, DOI: 10.1007/978-3-031-38004-4.

8 S. Wu, Y. Wang, M. Iqbal, K. Mehmood, Y. Li, Z. Tang, *et al.*, Challenges of fluoride pollution in environment: Mechanisms and pathological significance of toxicity – A review, *Environ. Pollut.*, 2022, DOI: 10.1016/j.envpol.2022.119241.

9 J. Podgorski and M. Berg, Global analysis and prediction of fluoride in groundwater, *Nat. Commun.*, 2022, **13**, 4232, DOI: 10.1038/s41467-022-31940-x.

10 K. W. Taylor, S. E. Eftim, C. A. Sibrizzi, R. B. Blain, K. Magnuson and P. A. Hartman, Fluoride Exposure and Children's IQ Scores: A Systematic Review and Meta-Analysis, *JAMA Pediatr.*, 2025, **179**(3), 282–292, DOI: 10.1001/jamapediatrics.2024.5542.

11 L. Plaza, M. Castellote, R. Nevshupa and E. Jimenez-Relinque, High-capacity adsorbents from stainless steel slag for the control of dye pollutants in water, *Environ. Sci. Pollut. Res.*, 2021, **18**, 23896–23910, DOI: 10.1007/s11356-020-12174-0/Published.

12 C. Shi, X. Wang, S. Zhou, X. Zuo and C. Wang, Mechanism, application, influencing factors and environmental benefit assessment of steel slag in removing pollutants from water: A review, *J. Water Proc. Eng.*, 2022, **47**, 102666, DOI: 10.1016/j.jwpe.2022.102666.

13 F. Obar, M. Alherbawi, G. Mckay and T. Al-Ansari, Optimizing the utilization of biochar from waste: an energy–water–food nexus assessment approach considering water treatment and soil application scenarios, *Front. Environ. Sci.*, 2023, **11**, 1238810, DOI: 10.3389/fenvs.2023.1238810.

14 M. S. Akhtar, S. Ali and W. Zaman, Recent Advancements in Catalysts for Petroleum Refining, *Catalysts*, 2024, DOI: 10.3390/catal14120841.

15 C. R. Baek, H. D. Kim and Y. C. Jang, Exploring glass recycling: Trends, technologies, and future trajectories, *Environ. Eng. Res.*, 2025, 1–16, DOI: 10.4491/eer.2024.241.
16 B. E. Akorley, O. B. Apea and G. A. Tiruye, Efficient water defluoridation and phosphate removal using recycled alkali-activated glass-calcium composites: Mechanisms and optimization, *Chem. Eng. J. Adv.*, 2026, **25**, 100975, DOI: 10.1016/j.ceja.2025.100975.
17 M. Mahmoud, J. Kraxner, A. Mehta and H. Elsayed, Upcycling waste derived glass into high-performance photocatalytic scaffolds by alkali activation and direct ink writing, *Heliyon*, 2024, **10**, 1–7, DOI: 10.1016/j.heliyon.2024.e24737.
18 M. Mahmoud, J. Kraxner, A. Mehta, H. Elsayed and E. Bernardo, Alkali activation-induced cold consolidation of waste glass : Application in organic-free direct ink writing of photocatalytic dye destructors, *J. Eur. Ceram. Soc.*, 2023, 1–11, DOI: 10.1016/j.jeurceramsoc.2023.12.023.
19 A. Mehta, K. Karbouche, J. Kraxner, H. Elsayed, D. Galusek and E. Bernardo, Upcycling of Pharmaceutical Glass into Highly Porous Ceramics: From Foams to Membranes, *Materials*, 2022, **15**(11), 1–13, DOI: 10.3390/ma15113784.
20 D. Lago, J. Kraxner, D. Galusek and E. Bernardo, Development of porous membranes by alkali activation of borosilicate glass: effect of wastewater acidity on copper adsorption, *Dev. Built Environ.*, 2025, **23**, 100705, DOI: 10.1016/j.dibe.2025.100705.
21 D. Lago, J. Kraxner, D. Galusek and E. Bernardo, Novel glass-based membranes for Cu adsorption: From alkali activation to sintering, *Heliyon*, 2023, **9**(8), e18221, DOI: 10.1016/j.heliyon.2023.e18221.
22 M. Mahmoud, J. Kraxner, H. Elsayed, D. Galusek and E. Bernardo, Advanced Dye Sorbents from Combined Stereolithography 3D Printing and Alkali Activation of Pharmaceutical Glass Waste, *Materials*, 2022, **15**(19), 6823, DOI: 10.3390/ma15196823.
23 S. A. Samad, A. Arafat, E. Lester and I. Ahmed, Upcycling Glass Waste into Porous Microspheres for Wastewater Treatment Applications: Efficacy of Dye Removal, *Materials*, 2022, **15**(17), 5809, DOI: 10.3390/ma15175809.
24 M. Mahmoud, J. Kraxner, H. Elsayed, F. M. Stabile, M. Michálková, D. Galusek, *et al.*, Enhanced methylene blue adsorption by double alkali activation of highly porous glass microspheres prepared from waste glass, *J. Mater. Sci.*, 2024, **59**(1), 73–85, DOI: 10.1007/s10853-023-09207-7.
25 H. Al-kroom, H. A. Abdel-Gawwad, M. Abd Elrahman, S. Abdel-Aleem, M. Saad Ahmed and Y. F. Salama, Utilization of Foamed Glass as an Effective Adsorbent for Methylene Blue: Insights into Physicochemical Properties and Theoretical Treatment, *Materials*, 2023, **16**(4), 1412, DOI: 10.3390/ma16041412.
26 S. A. Samad, A. Arafat, E. Lester and I. Ahmed, Upcycling Glass Waste into Porous Microspheres for Wastewater Treatment Applications: Efficacy of Dye Removal, *Materials*, 2022, **15**(17), 1–26, DOI: 10.3390/ma15175809.
27 P. S. Guru, B. Panda and K. N. Parida, Adsorption of textile dyes on hydroxyapatite based adsorbent: A review of surface functionality and adsorption mechanism, *Next Mater.*, 2025, DOI: 10.1016/j.nxmate.2025.101042.
28 V. N. Scheverin, L. N. Schmidt, E. M. Diaz, M. F. Horst and V. L. Lassalle, Synthesis of hydroxyapatite-iron oxides nanocomposite for fluoride adsorption in groundwater samples, *Environ. Geochem. Health*, 2025, **47**(9), 383, DOI: 10.1007/s10653-025-02702-7.
29 J. P. Raval, P. Joshi, D. R. Chejara and I. A. Disher, Fabrication and applications of hydroxyapatite-based nanocomposites coating for bone tissue engineering, in. *Applications of Nanocomposite Materials in Orthopedics*, 2019, pp, 71–82, DOI: 10.1016/B978-0-12-813740-6.00004-1.
30 A. Hatim, D. Khaddoudi, F. Abida, H. Ait Ali Ouydir, S. Kouzbour and M. Agunaou, Low-cost and sustainable hydroxyapatite synthesis using technical-grade phosphoric acid for environmental applications: Structural and morphological insights, *Open Ceram.*, 2025, **24**, 100870, DOI: 10.1016/j.oceram.2025.100870.
31 M. Montesissa, V. Tommasini, K. Rubini, M. Boi, N. Baldini and E. Boanini, State of Art and Perspective of Calcium Phosphate-Based Coatings Coupled with Bioactive Compounds for Orthopedic Applications, *Nanomaterials*, 2025, DOI: 10.3390/nano15151199.
32 V. Naubnome, A. Prihanto, W. W. Schmahl, Y. M. Pusparizkita, R. Ismail and J. Jamari, Chemical precipitation of nanocrystalline hydroxyapatite with calcium carbonate derived from green mussel shell wastes and several phosphorus sources, *Case Stud. Chem. Environ. Eng.*, 2025, **11**, 101154, DOI: 10.1016/j.cscee.2025.101154.
33 C. A. Moras, L. T. Bach, T. Cyronak, R. Joannes-Boyau and K. G. Schulz, Ocean alkalinity enhancement - avoiding runaway CaCO3 precipitation during quick and hydrated lime dissolution, *Biogeosciences*, 2022, **19**(15), 3537–3557, DOI: 10.5194/bg-19-3537-2022.
34 M. Benbouda, D. Boudemagh, D. Chebli and H. Ounoughi, Fluorapatite: A Comprehensive Review of Synthesis, Biological Properties, and Environmental Applications, *ChemistrySelect*, 2025, DOI: 10.1002/slct.202501978.
35 G. George and G. Karunanidhi, The role of various composites on pristine hydroxyapatite for the enhanced adsorption of heavy metal ions: A review, *Results Surf. Interfaces*, 2025, DOI: 10.1016/j.rsurfi.2025.100663.
36 C. O. Onyegbado, E. T. Iyagba and O. J. Offor, Solid Soap Production using Plantain Peel Ash as Source of Alkali, *J. Appl. Sci. Environ. Manag.*, 2002, **6**(1), 73–77.
37 J. Undiandeye, B. S. Vopnu, B. O. Evbuomwan and K. H. Amakiri, Assessment of alkali levels in palm bunch ash, for black soap production, *Eur. Int. J. Sci. Technol.*, 2015, **4**(8), 138–142. Available from:https://eijst.org.uk/.
38 J. Gómez-Morales, J. Torrent-Burgués, T. Boix, J. Fraile and R. Rodríguez-Clemente, Precipitation of stoichiometric hydroxyapatite by a continuous method, *Cryst. Res. Technol.*, 2001, **36**(1), 15–26, DOI: 10.1002/1521-4079(200101)36:1<15::AID-CRAT15>3.0.CO;2-E.

39 G. Uehara, G. P. Gillman, Analytical Methods. In "*The Mineralogy, Chemistry, and Physics of Tropical Soils with Variable Charge Clays*. Westview Tropical Agriculture Series. Westview Press, Boulder, Colorado, 1981.

40 A. Demirbas, E. Pehlivan, F. Gode, T. Altun and G. Arslan, Adsorption of Cu(II), Zn(II), Ni(II), Pb(II), and Cd(II) from aqueous solution on Amberlite IR-120 synthetic resin, *J. Colloid Interface Sci.*, 2005, **282**(1), 20–25, DOI: 10.1016/j.jcis.2004.08.147.

41 S. Edebali and E. Pehlivan, Evaluation of Cr(III) by ion-exchange resins from aqueous solution: equilibrium, thermodynamics and kinetics, *Desalination Water Treat.*, 2014, **52**(37–39), 7143–7153, DOI: 10.1080/19443994.2013.821631.

42 P. Saha, S. Chowdhury, in. *Insight into Adsorption Thermodynamics*, ed. Prof. Mizutani T.. Rijeka. InTech, 2011, pp. 350–362, Available from: https://www.intechopen.com/book/thermodynamics/insight-into-adsorption-thermodynamics.

43 A. Dabagh, R. Benhiti, M. EL-Habacha, A. Ait Ichou, M. Abali and A. Assouani, Application of Taguchi method, response surface methodology, DFT calculation and molecular dynamics simulation into the removal of orange G and crystal violet by treated biomass, *Heliyon*, 2023, **9**(11), e21977, DOI: 10.1016/j.heliyon.2023.e21977.

44 M. Benjelloun, Y. Miyah, S. Ssouni, S. Iaich, M. El-habacha and S. Lagdali, Capparis spinosa L waste activated carbon as an efficient adsorbent for crystal violet toxic dye removal: Modeling, optimization by experimental design, and ecological analysis, *Chin. J. Chem. Eng.*, 2024, **71**, 283–302, DOI: 10.1016/j.cjche.2024.04.010.

45 Y. Miyah, S. Ssouni, M. Benjelloun, F. Mejbar, M. El-Habacha and S. Iaich, DFT theoretical analysis and experimental approach combination to understand the toxic dye's adsorption mechanism on the corncob-activated carbon surface, *J. Mol. Struct.*, 2023, **1288**, 135742, DOI: 10.1016/j.molstruc.2023.135742.

46 A. A. Acosta-Herrera, V. Hernández-Montoya, F. Castillo-Borja, M. A. Pérez-Cruz, M. A. Montes-Morán and F. J. Cervantes, Competitive adsorption of pollutants from anodizing wastewaters to promote water reuse, *J. Environ. Manage.*, 2021, **293**, 112877, DOI: 10.1016/j.jenvman.2021.112877.

47 W. Shi, M. Yi, Y. Liu, S. Huang, J. Fan and P. N. L. Lens, Preparation of hydroxyapatite (HAP) from waste eggshells for enhancing the granulation and treatment performance of aerobic granular sludge: Enhancement effects and mechanism insights, *Chem. Eng. J.*, 2023, **477**, 147096, DOI: 10.1016/j.cej.2023.147096.

48 R. Verma, S. R. Mishra, V. Gadore and M. Ahmaruzzaman, Hydroxyapatite-based composites: Excellent materials for environmental remediation and biomedical applications, *Adv. Colloid Interface Sci.*, 2023, **315**(7), 102890, DOI: 10.1016/j.cis.2023.102890.

49 Y. Chen, Q. Chen, R. M. Kasomo, Y. Jin, P. Yang and H. Zheng, Adsorption of fluoride from aqueous solutions using graphene oxide composite materials at a neutral pH, *J. Mol. Liq.*, 2023, **377**, 121467, DOI: 10.1016/j.molliq.2023.121467.

50 A. C. Carvalho, F. Raupp-Pereira, J. B. Rodrigues Neto and A. P. Novaes De Oliveira, A new source for production of ceramic filters, *Mater. Lett.*, 2015, **145**, 250–252, DOI: 10.1016/j.matlet.2015.01.131.

51 C. Noiriel, L. Luquot, B. Madé, L. Raimbault, P. Gouze and J. van der Lee, Changes in reactive surface area during limestone dissolution: An experimental and modelling study, *Chem. Geol.*, 2009, **265**(1–2), 160–170, DOI: 10.1016/j.chemgeo.2009.01.032.

52 J. Davidovits, in. *Geopolymer Chemistry and Applications*. 5th edn, Saint-Quentin, Institut Geopolymere, 2020, Available from: https://www.researchgate.net/publication/265076752.

53 G. D. Venkatasubbu, S. Ramasamy, V. Ramakrishnan and J. Kumar, Nanocrystalline hydroxyapatite and zinc-doped hydroxyapatite as carrier material for controlled delivery of ciprofloxacin, *3 Biotech.*, 2011, **1**(3), 173–186, DOI: 10.1007/s13205-011-0021-9.

54 A. Adesina, Durability and Microstructural Characteristics of Alkali Activated Materials Made with Waste Glass as Precursor: A Review, *Clean. Mater.*, 2022, DOI: 10.1016/j.clema.2022.100134.

55 E. A. Ofudje, A. Rajendran, A. I. Adeogun, M. A. Idowu, S. O. Kareem and D. K. Pattanayak, Synthesis of organic derived hydroxyapatite scaffold from pig bone waste for tissue engineering applications, *Adv. Powder Technol.*, 2018, **29**(1), 1–8, DOI: 10.1016/j.apt.2017.09.008.

56 N. I. Agbeboh, I. O. Oladele, O. O. Daramola, A. A. Adediran, O. O. Olasukanmi and M. O. Tanimola, Environmentally sustainable processes for the synthesis of hydroxyapatite, *Heliyon*, 2020, DOI: 10.1016/j.heliyon.2020.e03765.

57 M. B. Pinson, E. Masoero, P. A. Bonnaud, H. Manzano, Q. Ji and S. Yip, Hysteresis from multiscale porosity: Modeling water sorption and shrinkage in cement paste, *Phys. Rev. Appl.*, 2015, **3**(6), 064009, DOI: 10.1103/PhysRevApplied.3.064009.

58 J. O. Iji, F. B. Ibrahim, A. S. Argungu and D. O. Obada, Development and optimization of hydroxyapatite/kaolin-based ceramic materials as potential adsorbents for water purification, *Environ. Adv.*, 2023, **13**, 100419, DOI: 10.1016/j.envadv.2023.100419.

59 M. Bohner, B. L. G. Santoni and N. Döbelin, β-tricalcium phosphate for bone substitution: Synthesis and properties, *Acta Biomater.*, 2020, 23–41, DOI: 10.1016/j.actbio.2020.06.022.

60 J. E. Barralet, T. Gaunt, A. J. Wright, I. R. Gibson and J. C. Knowles, Effect of Porosity Reduction by Compaction on Compressive Strength and Microstructure of Calcium Phosphate Cement, *J. Biomed. Mater. Res.*, DOI: 10.1002/jbm.0000.

61 J. C. Mendez and T. Hiemstra, Ternary Complex Formation of Phosphate with Ca and Mg Ions Binding to Ferrihydrite: Experiments and Mechanisms, *ACS Earth Space Chem.*, 2020, **4**(4), 545–557, DOI: 10.1021/acsearthspacechem.9b00320.

62 B. Hosseini Monjezi, J. Lützenkirchen, *et al.*, Adsorption Behaviors of Lanthanum (III) and Yttrium (III) Ions on Gibbsite, *Minerals*, 2024, DOI: 10.3390/min14111137.
63 G. Mahmoudy, A. Dabagh, M. El-Habacha, S. Lagdali, A. Assouani and I. Soulaiman, Preparation and characterization of biomaterial for phosphate ion removal: Kinetics, isotherms and thermodynamics studies, *Desalination Water Treat.*, 2024, **317**, 100062, DOI: 10.1016/j.dwt.2024.100062.
64 P. Marin, C. E. Borba, A. N. Módenes, F. R. Espinoza-Quiñones, S. P. D. De Oliveira and A. D. Kroumov, Determination of the mass transfer limiting step of dye adsorption onto commercial adsorbent by using mathematical models, *Environ. Technol.*, 2014, **35**(18), 2356–2364, DOI: 10.1080/09593330.2014.904445.
65 B. K. Nandi, A. Goswami, A. K. Das, B. Mondal and M. K. Purkait, Kinetic and equilibrium studies on the adsorption of crystal violet dye using Kaolin as an adsorbent, *Sep. Sci. Technol.*, 2008, **43**(6), 1382–1403, DOI: 10.1080/01496390701885331.
66 O. B. Apea, B. E. Akorley, E. O. Oyelude and B. Ampadu, Evaluation of the adsorption behavior and divalent metal ions removal efficiency of ceramic point-of-use water filter materials, *Environ. Syst. Res.*, 2023, **12**, 37, DOI: 10.1186/s40068-023-00322-7.
67 P. Loganathan, S. Vigneswaran, J. Kandasamy and R. Naidu, Defluoridation of drinking water using adsorption processes, *J. Hazard. Mater.*, 2013, 1–19, DOI: 10.1016/j.jhazmat.2012.12.043.
68 L. Zhou, Q. Yu, Y. Cui, F. Xie, W. Li, Y. Li, *et al.*, Adsorption properties of activated carbon from reed with a high adsorption capacity, *Ecol. Eng.*, 2017, **102**, 443–450, DOI: 10.1016/j.ecoleng.2017.02.036.
69 S. M. Momina and S. Isamil, Regeneration performance of clay-based adsorbents for the removal of industrial dyes: A review, *RSC Adv.*, 2018, **8**(43), 24571–24587, DOI: 10.1039/c8ra04290j.
70 S. Thakur, S. Singh and B. Pal, Superior adsorption removal of dye and high catalytic activity for transesterification reaction displayed by crystalline CaO nanocubes extracted from mollusc shells, *Fuel Process. Technol.*, 2021, **213**, 106707, DOI: 10.1016/j.fuproc.2020.106707.
71 Y. Zhao, J. Geng, X. Wang, X. Gu and S. Gao, Tetracycline adsorption on kaolinite: PH, metal cations and humic acid effects, *Ecotoxicology*, 2011, **20**(5), 1141–1147, DOI: 10.1007/s10646-011-0665-6.
72 S. Aytas, M. Yurtlu and R. Donat, Adsorption characteristic of U(VI) ion onto thermally activated bentonite, *J. Hazard. Mater.*, 2009, **172**(2–3), 667–674, DOI: 10.1016/j.jhazmat.2009.07.049.
73 S. Ismadji, F. E. Soetaredjo and A. Ayucitra, Natural Clay Minerals as Environmental Cleaning Agents, in *Clay Materials for Environmental Remediation*, SpringerBriefs in Molecular Science, Springer, Cham, 2015, DOI: 10.1007/978-3-319-16712-1_2.
74 M. Benjelloun, Y. Miyah, G. Akdemir Evrendilek, F. Zerrouq and S. Lairini, Recent Advances in Adsorption Kinetic Models: Their Application to Dye Types, *Arab. J. Chem.*, 2021, **14**, 202104, DOI: 10.1016/j.arabjc.2021.103031.
75 P. Zhang, M. He, S. Huo, F. Li and K. Li, Recent progress in metal-based composites toward adsorptive removal of phosphate: Mechanisms, behaviors, and prospects, *Chem. Eng. J.*, 2022, **446**(2), 137081, DOI: 10.1016/j.cej.2022.137081.
76 D. Yang, Y. Li, L. Zhao, F. Cheng, L. Chang and D. Wu, Constructing ZIF-8-decorated montmorillonite composite with charge neutralization effect and pore structure optimization for enhanced Pb2+ capture from water, *Chem. Eng. J.*, 2023, **466**, 143014, DOI: 10.1016/j.cej.2023.143014.
77 Y. Zou, Y. Wang, J. Wang, S. Wang, L. Chen and Y. Xi, Preparation of hydroxyapatite and its elimination of excess fluoride from aqueous solution, *RSC Adv.*, 2024, **14**(36), 26103–26114, DOI: 10.1039/d4ra02147a.
78 R. Boteju, L. Zheng, H. M. S. Wasana, Q. Wu, Y. Wei and H. Zhong, Hydroxyapatite-Modified Zeolite for Fluoride Removal from Drinking Water: Adsorption Mechanism Investigation and Column Study, *Water*, 2025, **17**(6), 908, DOI: 10.3390/w17060908.
79 H. Bahmani and D. Mostofinejad, Microstructural characterization of alkali-activated concrete using waste-derived activators from industrial and agricultural sources: A review, *Case Stud. Constr. Mater.*, 2025, **22**, e04632, DOI: 10.1016/j.cscm.2025.e04632.
80 J. Wang, D. Shi, M. Liu, K. Yu, Y. Zhao and Y. Xia, Low-carbon alkali-activated materials for Cu(II)-contaminated soil stabilization: Reaction kinetics, immobilization mechanisms, and leaching behavior, *Case Stud. Constr. Mater.*, 2025, **23**, e04912, DOI: 10.1016/j.cscm.2025.e04912.
81 C. Ruiz-Aguilar, Porous phosphate-based bioactive glass/β-TCP scaffold for tooth remineralization, *PLoS One*, 2023, **18**(5), e0284885, DOI: 10.1371/journal.pone.0284885.
82 S. Singh, G. Murugesan, R. Vinayagam, T. Varadavenkatesan and R. Selvaraj, Adsorptive removal of fluoride from water using hydroxyapatite synthesized from marine shell waste, *Sci. Rep.*, 2025, **15**, 25598, DOI: 10.1038/s41598-025-11132-5.
83 M. Hashemkhani, M. Rezvani Ghalhari, P. Bashardoust, S. S. Hosseini, A. Mesdaghinia and A. H. Mahvi, Fluoride removal from aqueous solution via environmentally friendly adsorbent derived from seashell, *Sci. Rep.*, 2022, **12**, 9655, DOI: 10.1038/s41598-022-13756-3.
84 T. L. Tan, P. A. Krusnamurthy, H. Nakajima and S. A. Rashid, Adsorptive, kinetics and regeneration studies of fluoride removal from water using zirconium-based metal organic frameworks, *RSC Adv.*, 2020, **10**(32), 18740–18752, DOI: 10.1039/d0ra01268h.
85 L. Gómez-Hortigüela, J. Pérez-Pariente, R. García, Y. Chebude and I. Díaz, Natural zeolites from Ethiopia for elimination of fluoride from drinking water, *Sep. Purif. Technol.*, 2013, **120**, 224–229, DOI: 10.1016/j.seppur.2013.10.006.
86 M. N. Sepehr, V. Sivasankar, M. Zarrabi and M. Senthil Kumar, Surface modification of pumice enhancing its fluoride adsorption capacity: An insight into kinetic and thermodynamic studies, *Chem. Eng. J.*, 2013, **228**, 192–204, DOI: 10.1016/j.cej.2013.04.089.

87 M. Mohapatra, D. Hariprasad, L. Mohapatra, S. Anand and B. K. Mishra, Mg-doped nano ferrihydrite - A new adsorbent for fluoride removal from aqueous solutions, *Appl. Surf. Sci.*, 2012, **258**(10), 4228–4236, DOI: 10.1016/j.apsusc.2011.12.047.

88 M. Mohapatra, D. Hariprasad, L. Mohapatra, S. Anand and B. K. Mishra, Mg-doped nano ferrihydrite - A new adsorbent for fluoride removal from aqueous solutions, *Appl. Surf. Sci.*, 2012, **258**(10), 4228–4236, DOI: 10.1016/j.apsusc.2011.12.047.